

Strain-tuned quantum criticality in electronic Potts-nematic systems

Anzumaan R. Chakraborty and Rafael M. Fernandes

School of Physics and Astronomy, University of Minnesota, Minneapolis, Minnesota 55455, USA

(Received 2 March 2023; revised 2 May 2023; accepted 3 May 2023; published 19 May 2023)

Motivated by recent observations of threefold rotational symmetry breaking in twisted moiré systems, cold-atom optical lattices, quantum Hall systems, and triangular antiferromagnets, we phenomenologically investigate the strain-temperature phase diagram of the electronic 3-state Potts-nematic order. While in the absence of strain the quantum Potts-nematic transition is first order, quantum critical points (QCP) emerge when uniaxial strain is applied, whose nature depends on whether the strain is compressive or tensile. In one case, the nematic amplitude jumps between two nonzero values while the nematic director remains pinned, leading to a symmetry-preserving metanematic transition that terminates at a quantum critical end point. For the other type of strain, the nematic director unlocks from the strain direction and spontaneously breaks an in-plane twofold rotational symmetry, which in twisted moiré superlattices triggers an electric polarization. Such a piezoelectric transition changes from first to second order upon increasing strain, resulting in a quantum tricritical point. Using a Hertz-Millis approach, we show that these QCPs share interesting similarities with the widely studied Ising-nematic QCP. The existence of three minima in the nematic action also leaves fingerprints in the strain-nematic hysteresis curves, which display multiple loops. At nonzero temperatures, because the upper critical dimension of the 3-state Potts model is smaller than three, the Potts-nematic transition is expected to remain first order in three dimensions, but to change to second order in two dimensions (2D). As a result, the 2D strain-temperature phase diagram displays two first-order transition wings bounded by lines of critical end points or tricritical points, reminiscent of the phase diagram of metallic ferromagnets. We discuss how our results can be used to unambiguously identify spontaneous Potts-nematic order.

DOI: [10.1103/PhysRevB.107.195136](https://doi.org/10.1103/PhysRevB.107.195136)**I. INTRODUCTION**

Electronic nematicity, which consists of the electronically driven breaking of the discrete rotational symmetry of a system [1], has been observed in various correlated electronic materials, including three families of unconventional superconductors: cuprates [2–4], heavy-fermion compounds [5–7], and iron-based materials [8–11]. In all those cases, the underlying tetragonal lattice renders the electronic nematic order parameter Ising like [12], as the system must select between two nearest-neighbor (or next-nearest-neighbor) bonds of the square lattice, which are related by a 90° rotation. The selected bond will either expand or contract since nematic order necessarily triggers a lattice distortion [9]. Conversely, application of uniaxial strain along one of the bond directions completely lifts the degeneracy between the two bonds, leading to a smearing of the nematic phase transition. The situation is analogous to the case of an Ising ferromagnet in the presence of a longitudinal magnetic field since strain acts as a conjugate field to the nematic order parameter. Due to the ubiquitous presence of residual and random strain in crystals [13–15], this property can make it experimentally challenging to distinguish whether an anisotropic property is due to spontaneous nematic order, nematic order induced by strain (perhaps associated with an enhanced nematic susceptibility), or simply strain [16]. More broadly, the intrinsic coupling between electronic nematicity and uniaxial strain gives rise to a rich phenomenology [17–20].

Recently, electronic nematic order has also been observed in systems whose underlying lattices have threefold rotational symmetry (i.e., triangular, honeycomb, and kagome), such as the hexagonal (111) surface of bismuth subjected to large magnetic fields [21], the trigonal lattice of the doped topological insulator Bi_2Se_3 [22,23], the triangular antiferromagnet $\text{Fe}_{1/3}\text{NbS}_2$ [24], a triangular optical lattice of cold ^{87}Rb atoms [25], and the triangular moiré superlattices of twisted bilayer graphene (TBG) [26–29], twisted double-bilayer graphene (TDBG) [30], twisted trilayer graphene [31], and heterobilayer transition metal dichalcogenides [32]. More broadly, Potts nematicity has been proposed to emerge in diverse settings, from frustrated magnets [33–37] to interacting moiré systems [38–50] and kagome metals [51]. In contrast to the case of lattices with fourfold rotational symmetry, the nematic order parameter here has a 3-state Potts character [52,53], corresponding to selecting one among three nearest-neighbor bonds related by a 120° (or 60°) rotation. The linear coupling between such a Potts-nematic order parameter and in-plane strain has been recently explored in different contexts [24,29,42,52,54–58]. An interesting result is that application of uniaxial strain along one of the bond directions may not fully lift the degeneracy between the three bonds. Consequently, unlike the case of a tetragonal lattice, a nematic-related transition, dubbed nematic-flop transition in Ref. [42], can take place in a triangular lattice even in the presence of uniaxial strain. The situation is analogous to a 3-state Potts ferromagnet in the

presence of an external magnetic field that points along one of the three allowed magnetic moment directions [59,60]. If a “positive” field is applied, i.e., a field that favors one of the moment directions, no additional symmetries can be spontaneously broken. However, if a “negative” field is applied, i.e., a field that penalizes one of the moment directions, there is a residual Ising symmetry associated with the two remaining moment directions. Such a symmetry is spontaneously broken in the vicinity of the zero-field ferromagnetic transition.

Another peculiarity of the 3-state Potts model is that its upper critical dimension is $d_u^{\text{Potts}} \lesssim 3$ (for a review, see Ref. [61]), whereas in the Ising model, $d_u^{\text{Ising}} = 4$. Most importantly, the character of the 3-state Potts transition is fundamentally different for dimensions above and below d_u^{Potts} . For $d \geq 3$, a mean-field description works and the transition is first order, due to the existence of a cubic invariant in the Landau free-energy expansion. However, for $d = 2$, the 3-state Potts transition is second order. This has important consequences for two-dimensional systems subjected to a 3-state Potts nematic instability, such as twisted moiré systems. At high enough temperatures, $d = 2$ and one expects a second-order nematic transition. However, at $T = 0$, since $d + z > d_u^{\text{Potts}}$ for the expected values of the dynamic critical exponent z (i.e., $z = 1$ for an insulator and $z = 3$ for a metal [62]), the nematic transition should be first order. This not only implies the absence of a Potts-nematic quantum critical point (QCP), but it also indicates that, as the nematic transition temperature is suppressed by a nonthermal tuning parameter, a tricritical point should emerge.

In this paper, we use a phenomenological model to study the Potts-nematic phase diagram in the presence of uniaxial strain. The nematic order parameter is parametrized as a two-component “vector” $\Phi = \phi(\cos 2\theta, \sin 2\theta)$, where ϕ is the magnitude and the director angle θ is restricted to three possible values. The tuning parameters are the temperature T and a nonthermal control parameter a , such as doping, which suppresses the Potts-nematic transition temperature to zero. Figure 1 summarizes our main findings for a two-dimensional (2D) system whose underlying lattice has threefold rotational symmetry. At $T = 0$, since the system is above the 3-state Potts upper critical dimension, it undergoes a first-order quantum nematic phase transition upon changing the nonthermal parameter a , where the threefold rotational symmetry C_{3z} is broken. The fate of the transition upon application of uniaxial strain along one of the nematic-bond directions depends on the sign of $\tilde{\varepsilon}$, which is linearly proportional to the strain ε , which in turn can be either compressive ($\varepsilon < 0$) or tensile ($\varepsilon > 0$).

For $\tilde{\varepsilon} < 0$, upon increasing the strain magnitude, a first-order transition line transition extends to larger a values, ending at a quantum critical end point (QCEP), analogously to the case of the liquid-gas transition of water. The magnitude of the nematic order parameter ϕ jumps across the first-order transition line, whereas the nematic director angle θ remains pinned by the strain direction, signaling a symmetry-preserving *quantum meta-nematic transition*. Beyond the QCEP, there is only a crossover signaled by the Widom line.

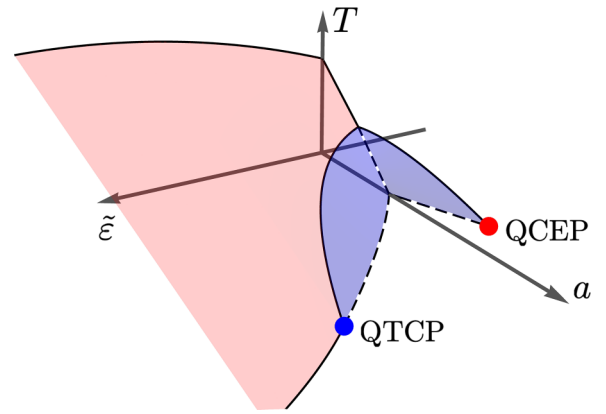


FIG. 1. Qualitative $(\tilde{\varepsilon}, a, T)$ phase diagram of a 2D Potts-nematic system, displaying first-order transition wings (blue surfaces). Here, a is a nonthermal tuning parameter like doping or pressure; $\tilde{\varepsilon}$ is linearly proportional to the uniaxial strain applied along one of the high-symmetry directions of the threefold rotationally symmetric lattice, but its sign depends on Landau coefficients of the Potts-nematic action. For $\tilde{\varepsilon} < 0$, the isolated wing of first-order transitions is bounded by a line of classical end points that terminates at a quantum critical end point (QCEP). No symmetries are broken across this metanematic transition. For $\tilde{\varepsilon} > 0$, the wing is bounded by a line of classical tricritical points terminating at a quantum tricritical point (QTCP), and is thus surrounded by a surface of continuous transitions (red surface). The in-plane twofold rotational symmetry is broken spontaneously across these transitions, giving rise to a piezoelectric phase in twisted moiré systems.

For $\tilde{\varepsilon} > 0$, while a first-order transition line extending to larger values of a also appears upon increasing the strain magnitude, the situation is completely different. The first key difference is that the director angle θ spontaneously unpins from the strain direction across the transition, selecting one among two possible angles, which in turn are related by twofold rotations with respect to in-plane axes (denoted by C'_2). Therefore, across this first-order Ising transition, the C'_2 symmetry is broken, resulting in the emergence of an out-of-plane ferroelectric polarization in the case of twisted moiré systems. Because this ferroelectricity only appears in the presence of strain of a particular type (compressive or tensile), we dub this a *quantum piezoelectric transition*. The second key difference with respect to the case of $\tilde{\varepsilon} < 0$ is that, upon applying stronger strain, the first-order transition line ends at a quantum tricritical point (QTCP), beyond which a line of piezoelectric QCPs emerges. A Hertz-Millis type of calculation for both the piezoelectric QCPs and the metanematic QCEP in the case of metallic systems reveals that they behave very similarly to an Ising-nematic QCP [63–69], not only possessing the same dynamical critical exponent $z = 3$, but also cold spots at the Fermi surface.

We also compute the upper and lower spinodal lines associated with the different first-order transition lines and employ a generalized Stoner-Wohlfarth approach [70] to show that the asymmetry between the effects of compressive and tensile strains is manifested in the hysteresis curves of $\Phi(\varepsilon)$. In particular, because there are three action minima available, rather than the usual two, the hysteresis curves can show multiple loops depending on the initial conditions. These characteristic

features of the hysteresis curves provide concrete criteria to unambiguously determine experimentally whether a twofold anisotropic signal observed in a system with threefold rotational symmetry is due to spontaneous nematic order or induced nematic order by strain.

The extension of the results to nonzero temperatures depends on the dimensionality of the system. For $d = 3$, the system is always above the 3-state Potts upper critical dimension, implying that the phase diagram at nonzero temperatures should be similar to that at $T = 0$. However, for $d = 2$, the Potts-nematic transition should generally become second order at high enough temperatures, thus displaying the typical critical exponents of the 2D 3-state Potts model [61]. Consequently, a tricritical point at $T \neq 0$ should exist for unstrained systems, connecting the first-order quantum phase transition to the second-order transition at high T . As illustrated in Fig. 1, this tricritical point is expected to directly connect to the QCEP and the QCTP, giving rise to two first-order transition wings. This shape of the phase diagram resembles that of an itinerant ferromagnet [71,72], although the mechanisms by which the $T = 0$ transition becomes first order are unrelated [73–75]. An important difference is that, in the Potts-nematic case, the first-order transition wing on the $\tilde{\varepsilon} < 0$ side is isolated, bounded by the line of critical end points, whereas the wing on the $\tilde{\varepsilon} > 0$ side is bounded by a line of tricritical points, and thus exists inside a much broader wing signaling the second-order transition to the piezoelectric phase.

The paper is organized as follows: In Sec. II we apply mean-field theory to determine the $T = 0$ phase diagram of the Potts-nematic model, focusing on the emergence of the metanematic QCEP and the piezoelectric QTCP in Secs. II B and II C, respectively. The Potts-nematic hysteresis curves are analyzed in Sec. III, whereas Sec. IV presents a qualitative analysis of the $T > 0$ phase diagram. Conclusions are presented in Sec. V.

II. ZERO-TEMPERATURE PHASE DIAGRAM

A. Mean-field solution of the Potts-nematic model

The “in-plane” nematic order parameter can always be parametrized as $\Phi \equiv (\phi_1, \phi_2) = \phi(\cos 2\theta, \sin 2\theta)$, where $\phi > 0$ is the magnitude and $0 \leq \theta \leq \pi$ is the nematic director angle [12,42]. By construction, the order parameter satisfies $\Phi(\theta) = \Phi(\theta + \pi)$, as is the case for the classical nematic order parameter. Physically, the components $\phi \cos 2\theta$ and $\phi \sin 2\theta$ transform as the expectation values of the electronic quadrupolar moments $\rho_{x^2-y^2}$ and ρ_{xy} , as well as the strain components $\varepsilon_{xx} - \varepsilon_{yy}$ and ε_{xy} . Here, $\varepsilon_{ij} = (\partial_i u_j + \partial_j u_i)/2$ is the strain tensor and \mathbf{u} the displacement vector. The allowed values of θ are constrained by the symmetries of underlying crystal lattice, as well as by the presence of in-plane uniaxial strain. Hereafter, we focus on lattices that are invariant under threefold rotations with respect to the z axis (C_{3z} operation) and twofold rotations with respect to at least one in-plane axis (C_2 operation). These include the triangular lattice as well as any other lattice with point groups D_{6h} , D_{3h} , D_{3d} , D_6 , and D_3 . Note that the latter two describe certain twisted moiré superlattices, like TBG and TDBG. We assume that external uniaxial strain is applied along a direction that makes an angle

α with respect to the x axis, and consider both tensile ($\varepsilon > 0$) and compressive ($\varepsilon < 0$) strain. In this case, the nematic action is given by [29,41,42,52]

$$S_{\text{nem}}[\Phi(q)] = \frac{1}{2} \int_q \phi_{-q} \chi_0^{-1}(q) \phi_q + \int_x \left[\frac{\lambda}{3} \phi^3 \cos 6\theta + \frac{u}{4} \phi^4 - \gamma \varepsilon \phi \cos(2\theta - 2\alpha) \right]. \quad (1)$$

Here, $x = (\tau, \mathbf{x})$ denotes imaginary time $\tau \in [0, \beta]$ and spatial variable \mathbf{x} , whereas $q = (\Omega_n, \mathbf{q})$ consists of bosonic Matsubara frequencies $\Omega_n = 2\pi nT$ and momentum \mathbf{q} . The inverse nematic susceptibility is given by $\chi_0^{-1}(q) = a + \mathbf{q}^2 + \Omega_n^2$, where a is a nonthermal tuning parameter. The coupling constants λ and $u > 0$ describe the nonharmonic terms of the action, whereas γ is the elastonematic coupling.

For $\varepsilon = 0$, the action (1) maps onto the 3-state Potts model or, equivalently, the three-state clock model. Indeed, for $\lambda > 0$, the nematic director is pinned to the three high-symmetry directions $\theta = (2n + 1)\pi/6$, whereas for $\lambda < 0$, the three allowed values are $\theta = 2n\pi/6$, with $n = 0, 1, 2$. In the presence of strain, there are important changes in the problem. In this paper, we consider strain applied along one of the high-symmetry directions of the lattice. In this case, we can set without loss of generality $\alpha = 2m\pi/6$ with $m = 0, 1, 2$, since the action (1) is invariant under $\varepsilon \rightarrow -\varepsilon$ and $\alpha \rightarrow \alpha + \pi/2$. This invariance reflects the fact that, for the nematic order parameter, compressive strain applied along one axis has the same effect as tensile strain applied along an orthogonal axis. Shifting the director angle such that it is measured with respect to the strain direction $\tilde{\theta} = \theta - \alpha$, and considering the case of static and homogeneous fields, the action “density” becomes

$$S_{\text{nem}}(\Phi) = \frac{a}{2} \phi^2 + \frac{u}{4} \phi^4 + \frac{\lambda}{3} \phi^3 \cos 6\tilde{\theta} - \gamma \varepsilon \phi \cos 2\tilde{\theta}. \quad (2)$$

Upon defining the rescaled quantities $\tilde{\phi} \equiv \frac{u}{|\lambda|} \phi$, $\tilde{S}_{\text{nem}} \equiv \frac{u^3}{\lambda^3} S_{\text{nem}}$, $\tilde{a} = \frac{u}{\lambda^2} a$, and $\tilde{\varepsilon} \equiv \frac{\gamma u^2}{\lambda^3} \varepsilon$, we can rewrite the action in a more convenient form

$$\tilde{S}_{\text{nem}} = \frac{\tilde{a}}{2} \tilde{\phi}^2 + \frac{1}{4} \tilde{\phi}^4 + \text{sgn} \lambda \left(\frac{1}{3} \tilde{\phi}^3 \cos 6\tilde{\theta} - \tilde{\varepsilon} \tilde{\phi} \cos 2\tilde{\theta} \right). \quad (3)$$

Regardless of whether the system is 2D or 3D, at $T = 0$ the effective dimensionality $d + z \geq 3$, implying that the system is above the upper critical dimension of the 3-state Potts model. As a result, a mean-field solution is appropriate; setting $\partial \tilde{S}_{\text{nem}} / \partial \tilde{\phi} = 0$ and $\partial \tilde{S}_{\text{nem}} / \partial \tilde{\theta} = 0$, and assuming $\tilde{\phi} \neq 0$, we find the mean-field equations

$$\tilde{a} \tilde{\phi} + \text{sgn} \lambda \tilde{\phi}^2 \cos 6\tilde{\theta} + \tilde{\phi}^3 = \text{sgn} \lambda \tilde{\varepsilon} \cos 2\tilde{\theta}, \quad (4)$$

$$\sin 6\tilde{\theta} = \frac{\tilde{\varepsilon}}{\tilde{\phi}^2} \sin 2\tilde{\theta}. \quad (5)$$

To make the notation less cumbersome, hereafter we drop the tilde of all quantities except for $\tilde{\varepsilon}$; the latter is to emphasize that the relevant quantity is the combination $\tilde{\varepsilon} = (\gamma u^2 / \lambda^3) \varepsilon$, whose overall sign depends not only on whether the applied strain ε is compressive or tensile, but also on the signs of

the nematicoelastic coupling γ and on the cubic Landau coefficient λ . We first review the well-known results in the case of no applied strain, $\tilde{\varepsilon} = 0$ [42,52]. Equation (5) gives the extrema $\theta_0 = p\pi/6$, with $p = 0, \dots, 5$. Computing the second derivative of the action at the extrema, we find $(\frac{\partial^2 S_{\text{nem}}}{\partial \theta^2})_{\theta_0} = -12\phi^3(-1)^p \text{sgn}\lambda$. Therefore, the minima (maxima) of the action are given by $\theta_0 = p\pi/6$ with even (odd) p if $\lambda < 0$ and odd (even) p if $\lambda > 0$. Meanwhile, Eq. (4) becomes

$$a - \phi_0 + \phi_0^2 = 0 \quad (6)$$

which gives

$$\phi_{0,\pm} = \frac{1}{2}(1 \pm \sqrt{1 - 4a}). \quad (7)$$

Clearly, a $\phi_0 \neq 0$ solution can only exist if $a < a_{\text{us}} \equiv \frac{1}{4}$, which sets the upper spinodal of the first-order Potts-nematic transition. The first-order transition takes place for $a \equiv a_{c,0}$ such that $S_{\text{nem}}(\phi_{0,+}, \theta_0) = 0$, which gives $a_{c,0} = \frac{2}{9}$. The jump in the nematic order parameter at the transition is thus given by $\Delta\phi_0 = \frac{2}{3}$.

The mean-field solution for nonzero strain has been in part discussed in Refs. [29,53] and, more broadly, in the literature of the 3-state Potts model under the presence of a magnetic field [59–61]. The second mean-field equation (5) can be rewritten as (where, we recall, the director angle θ is measured with respect to the direction strain is applied)

$$\sin 2\theta \left[\cos^2 2\theta - \frac{1}{4} \left(1 + \frac{\tilde{\varepsilon}}{\phi^2} \right) \right] = 0. \quad (8)$$

This equation always admits two solutions: $\theta_+ = 0$, corresponding to a nematic director parallel to the strain direction, and $\theta_- = \pi/2$, denoting a nematic director perpendicular to the strain direction. Note that, by definition, $\Phi \rightarrow -\Phi$ upon a rotation of 90° of the director angle θ . In both cases, the mean-field equation (4) that determines the ϕ_{\pm} values corresponding to θ_{\pm} is

$$a\phi_{\pm} + \phi_{\pm}^3 \pm \text{sgn}\lambda (\phi_{\pm}^2 - \tilde{\varepsilon}) = 0, \quad (9)$$

whereas the action evaluated at these extrema is given by

$$S_{\pm} = \frac{a}{2} \phi_{\pm}^2 + \frac{1}{4} \phi_{\pm}^4 \pm \text{sgn}\lambda \left(\frac{1}{3} \phi_{\pm}^3 - \tilde{\varepsilon} \phi_{\pm} \right). \quad (10)$$

To check which of these solutions (if any) is a minimum of the action, we evaluate the second derivative:

$$\left(\frac{\partial^2 S_{\text{nem}}}{\partial \theta^2} \right)_{\theta_{\pm}} = \pm 4 \text{sgn}\lambda \phi_{\pm} \tilde{\varepsilon} \left(1 - \frac{3\phi_{\pm}^2}{\tilde{\varepsilon}} \right). \quad (11)$$

It follows that, when $\tilde{\varepsilon} < 0$, the θ_- (θ_+) solution is always a local action minimum for $\lambda > 0$ ($\lambda < 0$). Meanwhile, when $\tilde{\varepsilon} > 0$, the situation is more involved. Far enough from the Potts-nematic transition of the unstrained system, where the nematic order parameter induced by the strain is expected to be small, $\phi^2 \ll \tilde{\varepsilon}$, we find that the θ_+ (θ_-) solution is a local minimum of the action for $\lambda > 0$ ($\lambda < 0$). Once the nematic order parameter increases such that $\phi^2 > \tilde{\varepsilon}/3$, however, this solution switches to a local maximum. This indicates that another solution is available. Indeed, the mean-field equation

for θ , Eq. (8), admits two additional solutions:

$$\theta_{\pm}^* = \pm \frac{1}{2} \arccos \left(\frac{1}{2} \sqrt{1 + \frac{\tilde{\varepsilon}}{\phi^2}} \right) \quad (12)$$

provided that the argument is smaller than 1, i.e., $\phi^2 > \tilde{\varepsilon}/3$. This is the same condition for which the θ_+ (θ_-) solution becomes a local maximum of the action for $\lambda > 0$ ($\lambda < 0$). Note that, in the director space spanned by the angle θ , the points θ_+^* and θ_-^* are related by a twofold rotation with respect to the horizontal axis (as well as the vertical axis), which indicates that selecting one of the two solutions will break a spatial symmetry of the system. We will return to this point later. Using Eq. (12), it is straightforward to obtain the mean-field equation for the corresponding nematic amplitude ϕ_{\pm}^*

$$a\phi_{\pm}^* + (\phi_{\pm}^*)^3 \mp \text{sgn}\lambda \phi_{\pm}^* \sqrt{\tilde{\varepsilon} + (\phi_{\pm}^*)^2} = 0 \quad (13)$$

as well as the values of the action evaluated at these solutions:

$$S_{\pm}^* = \frac{a}{2} (\phi_{\pm}^*)^2 + \frac{1}{4} (\phi_{\pm}^*)^4 \mp \frac{\text{sgn}\lambda}{3} [\tilde{\varepsilon} + (\phi_{\pm}^*)^2]^{3/2}. \quad (14)$$

Equation (13) can be solved in a straightforward way:

$$\phi_{\pm}^* = \sqrt{\frac{1}{2} - a \pm \sqrt{\tilde{\varepsilon} - a + \frac{1}{4}}}. \quad (15)$$

It turns out that the ϕ_{\pm}^* solution is either a saddle point of the action or does not satisfy the condition $\phi^2 < \tilde{\varepsilon}/3$. Consequently, ϕ_+^* is the desired solution, yielding

$$\theta_{\pm}^* = \pm \frac{1}{2} \arccos \left(\frac{1}{2} \left[1 + \frac{\tilde{\varepsilon}}{\frac{1}{2} - a + \sqrt{\tilde{\varepsilon} - a + \frac{1}{4}}} \right]^{1/2} \right). \quad (16)$$

We therefore obtain three different viable solutions for $\tilde{\varepsilon} \neq 0$: $\theta_+ = 0$, $\theta_- = \pi/2$, and θ_{\pm}^* given by Eq. (16). Following our analysis above, either θ_- or θ_+ is expected to be the global minimum for $\tilde{\varepsilon} < 0$, depending on whether $\lambda > 0$ or $\lambda < 0$, respectively. On the other hand, for $\tilde{\varepsilon} > 0$, two different minima are expected for distinct ranges of a : θ_+ or θ_- (for $\lambda > 0$ and $\lambda < 0$, respectively) and θ_{\pm}^* .

The full phase diagram can be directly obtained by comparing the actions evaluated at the three solutions, Eqs. (10) and (14), after solving for the corresponding nematic amplitude in Eqs. (9) and (16). The resulting phase diagram is shown in Fig. 2; as anticipated, it is analogous to the phase diagram of the ferromagnetic 3-state Potts model in the presence of a magnetic field [59,60]. For concreteness, we consider the case in which $\lambda > 0$. For $\tilde{\varepsilon} < 0$, we indeed find that the $\theta_- = \pi/2$ solution is the global minimum for any value of a . This does not mean, however, that the system does not undergo a phase transition. As denoted by the dashed line in Fig. 2, for small enough $|\tilde{\varepsilon}|$ and close enough to the nematic transition at zero strain, $a_c = \frac{2}{9}$, the system undergoes a symmetry-preserving first-order transition in which the nematic amplitude ϕ_- jumps, while the nematic director angle θ remains fixed. This is expected since the nematic order parameter undergoes a first-order transition in the absence of

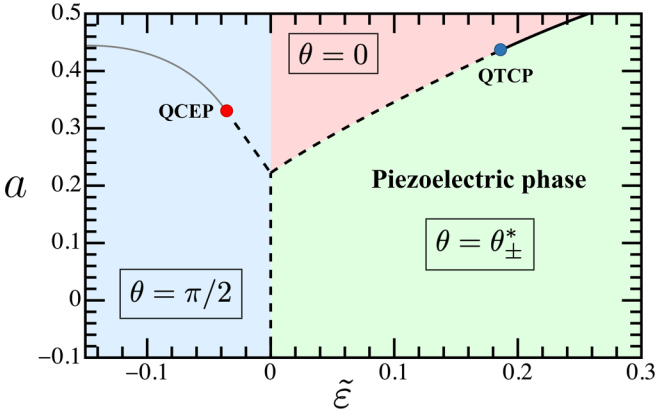


FIG. 2. Zero-temperature $(\tilde{\varepsilon}, a)$ phase diagram of a Potts-nematic system. The red and blue regions correspond to the phases in which the director angle θ is fixed to the high-symmetry directions $\theta_+ = 0$ and $\theta_- = \pi/2$, respectively, whereas the green region corresponds to the piezoelectric phase, in which $\theta = \theta_{\pm}^*$ is not fixed [see Eq. (12)]. For $\tilde{\varepsilon} < 0$, there is a first-order metanematic transition line (dashed black) that ends at a QCEP. Beyond the QCEP, there is a crossover signaled by the Widom line (solid gray). For $\tilde{\varepsilon} > 0$, the first-order piezoelectric transition, which spontaneously breaks in-plane twofold rotational symmetry, ends at a QTCP, after which it becomes second order (solid black line).

strain and $\tilde{\varepsilon}$ acts as a conjugate field to the nematic order parameter. We dub this a metanematic quantum phase transition, in analogy to the $T = 0$ metamagnetic transition that takes place in a metallic ferromagnet subjected to an external field. The first-order line ends in a critical end point, similarly to the liquid-gas transition of water. This side of the phase diagram is further discussed in Sec. II B.

The $\tilde{\varepsilon} > 0$ side of the phase diagram is qualitatively different. As displayed in Fig. 2, for $a \gg a_c$, the global minimum is at $\theta_+ = 0$. However, upon approaching the nematic transition point of the unstrained system, $a_{c,0} = \frac{2}{9}$, the nematic director angle that minimizes the action switches to θ_{\pm}^* . In contrast to the transition on the $\tilde{\varepsilon} < 0$ side of the phase diagram, this is not a symmetry-preserving transition since the spatial symmetry that relates the two nematic director angles θ_+^* and θ_-^* is spontaneously broken. For small enough $\tilde{\varepsilon}$, this transition is first order whereas for large enough $\tilde{\varepsilon}$, it becomes second order. Therefore, there is a tricritical point, marked in the figure, for intermediate values of $\tilde{\varepsilon}$. We will analyze this side of the phase diagram in more detail in Sec. II C.

The change in the nematic director angle upon decreasing a for $\tilde{\varepsilon} > 0$, discussed also in Ref. [42], can be understood directly from the action in Eq. (3). For $\lambda > 0$, the cubic term is minimized for $\theta = \pi/6, \pi/2, 5\pi/6$ and maximized for $\theta = 0, \pi/3, 2\pi/3$. The linear term, on the other hand, is minimized by $\theta = \pi/2$ and maximized by $\theta = 0$, for $\tilde{\varepsilon} < 0$, and minimized by $\theta = 0$ and maximized by $\theta = \pi/2$ for $\tilde{\varepsilon} > 0$. Therefore, in the regime $\tilde{\varepsilon} < 0$, both the linear and cubic terms can be simultaneously minimized by the same nematic director angle, $\theta = \pi/2$. In contrast, in the regime $\tilde{\varepsilon} > 0$, the minimum of the cubic term is the maximum of the linear term and vice versa. For large enough values of a , where the amplitude of the nematic order parameter is small, the linear

term wins over the cubic one. Once the system approaches its intrinsic nematic instability, the nematic amplitude increases and the two terms eventually give comparable contributions to the action. This frustration between the minima and maxima of the cubic and linear terms is lifted by a compromise value for the nematic director θ . Indeed, Eq. (12) for θ_{\pm}^* interpolates between 0 when $\phi^2 = \tilde{\varepsilon}/3$, which minimizes the linear term, to $\pi/6$ and $5\pi/6$ when $\phi^2 \gg \tilde{\varepsilon}/3$, which minimizes the cubic term.

B. Metanematic quantum critical end point

To gain further insight into the $\tilde{\varepsilon} < 0$ region of the phase diagram, we substitute the value of the nematic director angle that minimizes the action $\theta_- = \pi/2$ in Eq. (3); recall that we are considering $\lambda > 0$. We then obtain an action that depends only on the magnitude ϕ :

$$S_{\text{nem}}^{(\tilde{\varepsilon} < 0)}(\phi) = \frac{a}{2}\phi^2 + \frac{1}{4}\phi^4 - \frac{1}{3}\phi^3 + \tilde{\varepsilon}\phi. \quad (17)$$

To proceed, we recall that, for zero strain $\tilde{\varepsilon} = 0$, the system undergoes a first-order transition at $a_{c,0} = \frac{2}{9}$ in which the nematic order parameter jumps by $\Delta\phi_0 = \frac{2}{3}$. Therefore, it is convenient to introduce the shifted nematic order parameter $\delta\phi \equiv \phi - \Delta\phi_0/2$, as it effectively removes the cubic term above. We find

$$S_{\text{nem}}^{(\tilde{\varepsilon} < 0)}(\delta\phi) = \frac{A}{2}(\delta\phi)^2 + \frac{1}{4}(\delta\phi)^4 - H\delta\phi, \quad (18)$$

where we dropped a constant term and defined

$$A \equiv a - \frac{1}{3}, \quad (19)$$

$$H \equiv -\tilde{\varepsilon} - \frac{1}{3}(a - a_{c,0}). \quad (20)$$

Equation (18) is nothing but the Ising model in the presence of an external field H , widely employed to describe symmetry-preserving phase transitions, such as the Mott transition [76,77] and certain magnetic transitions [78]. It consists of a first-order transition line parametrized by $H = 0$, below which the order parameter ϕ jumps between two nonzero values, signaling a meta-nematic transition. The first-order transition line, and thus the jump in ϕ , terminates at the so-called critical end point, given by $A = H = 0$, which in our case is a quantum critical end point (QCEP), since the system is at $T = 0$. This allows us to obtain the location of the QCEP in the $(\tilde{\varepsilon}, a)$ phase diagram

$$a_{\text{QCEP}} = \frac{1}{3}, \quad (21)$$

$$\tilde{\varepsilon}_{\text{QCEP}} = -\frac{1}{27} \quad (22)$$

as well as the equation describing the first-order transition line:

$$a_c(\tilde{\varepsilon}) = \frac{2}{9} - 3\tilde{\varepsilon} \quad \text{for } \tilde{\varepsilon}_{\text{QCEP}} < \tilde{\varepsilon} < 0. \quad (23)$$

The behavior of the magnitude of the nematic order parameter ϕ and of the nematic component projected along the strain direction $\phi_1 = \phi \cos 2\theta$ is shown in Fig. 3 as a function of the nonthermal tuning parameter a for fixed values of strain $\tilde{\varepsilon} < 0$. For $\tilde{\varepsilon} < \tilde{\varepsilon}_{\text{QCEP}}$, as shown in Figs. 3(a) and 3(b), the nematic order parameter evolves continuously and displays a

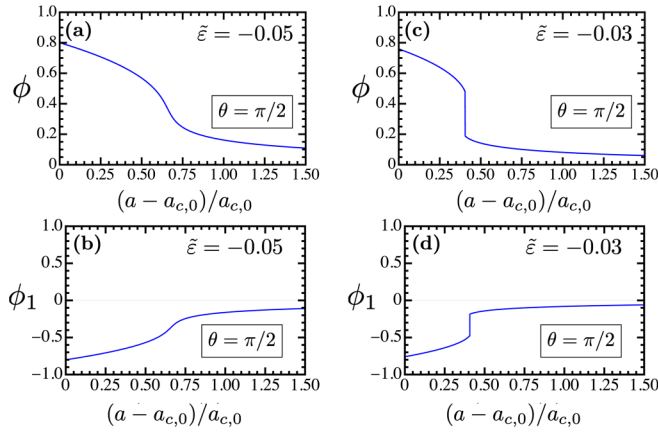


FIG. 3. Behavior of the nematic order parameter for fixed $\tilde{\varepsilon} < 0$ across the crossover Widom line [(a) and (b)] and the metanematic transition line [(c) and (d)], as defined in the phase diagram of Fig. 2. Representative values of $\tilde{\varepsilon}$ are chosen from the left and right side of $\tilde{\varepsilon}_{\text{QCEP}} = -\frac{1}{27} \approx -0.037$, respectively. The top panels show the magnitude of the nematic order parameter ϕ and the bottom panels, the nematic component projected along the strain direction, $\phi_1 = \phi \cos 2\theta$; in all cases, the nematic director angle remains fixed at $\pi/2$. The horizontal axis corresponds to the nonthermal tuning parameter a measured relative to unstrained Potts-nematic transition point $a_{c,0} = \frac{2}{9}$.

crossover behavior at a characteristic a value corresponding to the Widom line located at the left of the QCEP. On the other hand, for $\tilde{\varepsilon} > \tilde{\varepsilon}_{\text{QCEP}}$, the nematic order parameter undergoes a jump between two nonzero values, signaling a symmetry-preserving metanematic transition, as shown in Figs. 3(c) and 3(d).

To characterize the properties of the QCEP, we calculate the dynamical critical exponent z . For an insulator, the bare dynamics of the nematic susceptibility $\chi_0(q)$ is unchanged by the coupling to the electrons, resulting in $z = 1$. For a metal, we employ a Hertz-Millis approach [62,79,80] to compute the one-loop polarization bubble $\Pi(q)$ that renormalizes the nematic susceptibility $\chi^{-1}(q) = \chi_0^{-1}(q) - \Pi(q)$. As discussed elsewhere [41,42], for a single-band system, the interaction (with coupling constant g) between the nematic field Φ and the electronic quadrupolar charge density is given by the Hamiltonian

$$H_I = g\phi \sum_{\mathbf{k}} \cos(2\beta_{\mathbf{k}} - 2\theta) c_{\mathbf{k}+q/2,\sigma}^\dagger c_{\mathbf{k}-q/2,\sigma}, \quad (24)$$

where $\tan \beta_{\mathbf{k}} \equiv k_y/k_x$ and the annihilation operator $c_{\mathbf{k},\sigma}$ refers to an electron with momentum \mathbf{k} and spin σ . Spin indices are implicitly summed. Recall that, in our notation, θ is measured with respect to the strain direction α . Therefore, it is convenient to define $\tilde{\beta}_{\mathbf{k}} \equiv \beta_{\mathbf{k}} - \alpha$. The coupled nematic-electronic action is then given by

$$\begin{aligned} \mathcal{S}[\Phi, \psi, \psi^\dagger] = & \mathcal{S}_{\text{nem}}[\Phi] + \int_{\mathbf{k}} (-i\omega_n + \xi_{\mathbf{k}}) \psi_{\mathbf{k}\sigma}^\dagger \psi_{\mathbf{k}\sigma} \\ & + g \int_{\mathbf{k},q} \phi_q \cos(2\tilde{\beta}_{\mathbf{k}} - 2\tilde{\theta}_q) \psi_{\mathbf{k}+q/2,\sigma}^\dagger \psi_{\mathbf{k}-q/2,\sigma}, \end{aligned} \quad (25)$$

where we reintroduced the tilde in $\tilde{\theta}$ for the sake of clarity. Here, ψ, ψ^\dagger are Grassmann variables, $\xi_{0,\mathbf{k}} = \epsilon_{\mathbf{k}} - \mu$ is the electronic dispersion, and $k = (\omega_n, \mathbf{k})$, where $\omega_n = 2\pi(n + 1/2)k_B T$ is the fermionic Matsubara frequency. In the $\tilde{\varepsilon} < 0$ side of the phase diagram, the nematic director $\tilde{\theta}$ is fixed at $\tilde{\theta}_- = \pi/2$. Therefore, in terms of $\delta\phi \equiv \phi - \Delta\phi_0/2$, the interacting action becomes

$$\mathcal{S}_{\text{int}} = -g \int_{\mathbf{k},q} \delta\phi_q \cos(2\tilde{\beta}_{\mathbf{k}}) \psi_{\mathbf{k}+q/2}^\dagger \psi_{\mathbf{k}-q/2}. \quad (26)$$

Moreover, the electronic dispersion is renormalized to $\xi_{\mathbf{k}} = \xi_{0,\mathbf{k}} - \frac{g}{3} \cos(2\tilde{\beta}_{\mathbf{k}})$, signaling the Fermi surface distortion caused by the nonzero nematic order parameter. The coupling in Eq. (26) is analogous to the case of a metal in the presence of an *Ising-nematic* QCP [63–66]. The lowering from 3-state Potts symmetry to Ising symmetry is due to the external strain pinning the nematic director. The residual Ising degree of freedom is not associated with any symmetry of the system, but a consequence of the fact that the transition in the absence of the conjugate field is first order. The situation is analogous to the QCEP of a metallic ferromagnet in the presence of a magnetic field [80].

It is now straightforward to compute the polarization bubble. To leading order in g , it is given by

$$\Pi(q) = -2g^2 \int_{\mathbf{k}} \cos^2(2\tilde{\beta}_{\mathbf{k}}) G_{0,\mathbf{k}+q/2} G_{0,\mathbf{k}-q/2}, \quad (27)$$

where $G_{0,\mathbf{k}}^{-1} = i\omega_n - \xi_{0,\mathbf{k}} + \frac{g}{3} \cos(2\tilde{\beta}_{\mathbf{k}})$ is the fermionic propagator for the distorted band dispersion. We find

$$\begin{aligned} \delta\Pi(q) = & -\frac{g^2}{2E_F} f_1\left(\frac{g}{3E_F}, \cos 2\tilde{\beta}_{\mathbf{q}}\right) \frac{|\Omega|}{v_F |\mathbf{q}|} \\ & - \frac{g^2}{2E_F} f_2\left(\frac{g}{3E_F}, \cos 2\tilde{\beta}_{\mathbf{q}}\right) \left(\frac{\Omega}{v_F |\mathbf{q}|}\right)^2, \end{aligned} \quad (28)$$

where E_F and v_F are the Fermi energy and the Fermi velocity of the undistorted Fermi surface, $\delta\Pi(q) \equiv \Pi(q) - \Pi(\mathbf{q}, \Omega = 0)$, and we defined the functions

$$f_1(\tilde{g}, x) = \frac{[(1 + \tilde{g}^2)x - 2\tilde{g}]^2}{\pi(1 - \tilde{g}^2)^{5/2}(1 - \tilde{g}x)^{5/2}}, \quad (29)$$

$$f_2(\tilde{g}, x) = \frac{4\tilde{g}(2 + \tilde{g}^2)x - 9\tilde{g}^2 - (2 + \tilde{g}^2)(2x^2 - 1)}{\pi(1 - \tilde{g}^2)^{5/2}(1 - \tilde{g}x)^3}. \quad (30)$$

Thus, as in the case of an *Ising-nematic* QCP, the Hertz-Millis dynamical critical exponent is $z = 3$ since $f_1(x) \geq 0$, except for the cold spots defined by $f_1(x_{\text{cs}}) = 0$. From Eq. (29), we find that the cold spots are located at

$$\tilde{\beta}_{\mathbf{q}} = \beta_{\mathbf{q}} - \alpha = \frac{1}{2} \arccos\left(\frac{6gE_F}{9E_F^2 + g^2}\right). \quad (31)$$

Due to the Fermi-surface distortion caused by the nonzero nematic order parameter, the cold spots shift away from the value $\tilde{\beta}_{\mathbf{q}} = \pm\pi/4$, which is recovered in the limit $g\Delta\phi \rightarrow 0$. Moreover, because $f_2(x_{\text{cs}}) > 0$, at the cold spots the dynamical critical exponent is given by $z = 2$.

C. Piezoelectric quantum tricritical point

We now move to the $\tilde{\varepsilon} > 0$ side of the $(\tilde{\varepsilon}, a)$ phase diagram. As discussed above, there are two different minima: $\theta_+ = 0$ far above a_c and θ_{\pm}^* , as given by Eq. (12), far below a_c . Our numerical results showed that the transition between the two corresponding phases is first order for small strain but second order for large strain. To understand this behavior analytically, we start from Eq. (3) and substitute $\phi = \sqrt{\frac{\tilde{\varepsilon}}{-1+4\cos^2 2\theta}}$ (recall that we are considering $\lambda > 0$). Near the QTCP, we can expand the action to leading order in θ . Dropping a constant term, we obtain

$$S_{\text{nem}}^{(\tilde{\varepsilon}>0)}(\theta) = \frac{\mathcal{A}}{2}\theta^2 + \frac{\mathcal{U}}{4}\theta^4 + \frac{\mathcal{W}}{6}\theta^6, \quad (32)$$

where we defined

$$\mathcal{A} \equiv \frac{16\tilde{\varepsilon}(3a - 2\sqrt{3\tilde{\varepsilon}} + \tilde{\varepsilon})}{27}, \quad (33)$$

$$\mathcal{U} \equiv \frac{64\tilde{\varepsilon}(18a - 13\sqrt{3\tilde{\varepsilon}} + 10\tilde{\varepsilon})}{81}, \quad (34)$$

$$\mathcal{W} \equiv \frac{64\tilde{\varepsilon}(1512a - 1183\sqrt{3\tilde{\varepsilon}} + 1224\tilde{\varepsilon})}{1215}. \quad (35)$$

The nematic order parameter in this case is given by

$$\phi = \sqrt{\frac{\tilde{\varepsilon}}{3}} \left(1 + \frac{8\theta^2}{3} \right). \quad (36)$$

Before analyzing the behavior of Eq. (32), let us discuss the nature of the phase transition from the $\theta_- = 0$ phase to the θ_{\pm}^* phase. In contrast to the $\tilde{\varepsilon} < 0$ case discussed in Sec. II B, here the emergent Ising degree of freedom θ is related to a symmetry of the system, namely, twofold rotations with respect to an in-plane axis C_2' . Indeed, as pointed out in Ref. [42], when the director moves away from the high-symmetry directions $p\pi/6$ (with $p = 1, \dots, 5$), which is the case only in the θ_{\pm}^* phase, the twofold rotational symmetry C_2' is spontaneously broken, in addition to the threefold rotational symmetry C_{3z} that is explicitly broken by the external strain.

More formally, focusing on a lattice with point group D_{6h} , strain applied along a high-symmetry direction lowers the point-group symmetry to D_{2h} . The onset of the θ_{\pm}^* phase breaks the in-plane twofold rotational symmetry, further lowering the point-group symmetry to C_{2h} . In the phase diagram of Fig. 2, starting from the $\tilde{\varepsilon} = 0$ axis slightly above the nematic transition point ($a > a_{c,0}$) and then increasing $\tilde{\varepsilon}$ (i.e., $\tilde{\varepsilon} > 0$), the sequence of point-group-symmetry lowering is $D_{6h} \rightarrow D_{2h} \rightarrow C_{2h}$. Importantly, while the first symmetry breaking is explicit and caused by any nonzero $\tilde{\varepsilon}$, the second one is spontaneous and requires a threshold value for $\tilde{\varepsilon}$. In contrast, upon decreasing $\tilde{\varepsilon}$ (i.e., $\tilde{\varepsilon} < 0$), there is only the explicit symmetry breaking $D_{6h} \rightarrow D_{2h}$ caused by

a nonzero $\tilde{\varepsilon}$. Following the same steps for the other point groups considered here, we find the following sequences of symmetry lowering upon increasing $\tilde{\varepsilon}$: $D_{3h} \rightarrow C_{2v} \rightarrow C_s$, $D_{3d} \rightarrow C_{2h} \rightarrow S_2, D_6 \rightarrow D_2 \rightarrow C_2$, and $D_3 \rightarrow C_2 \rightarrow C_1$.

This result becomes even more interesting in the case of lattices described by the point groups D_6 and D_3 , which lack any mirror symmetries. These are the groups that describe the symmetries of twisted bilayer graphene and twisted double-bilayer graphene. In these cases, spontaneous breaking of the in-plane twofold rotational symmetry in the θ_{\pm}^* phase results in the condensation of an electric polarization P_z pointing out of the plane. This can be seen by analyzing how the Potts-nematic order parameter couples to P_z in these groups. Following Ref. [81], the nematoelectric action is given by

$$S' = \frac{\Upsilon}{6} P_z \phi^3 \sin 6\theta = \frac{\Upsilon}{6} P_z \phi^3 \sin 6\tilde{\theta}, \quad (37)$$

where Υ is a coupling constant. Expanding for small θ , we find

$$S' \approx \Upsilon \left(\frac{\tilde{\varepsilon}}{3} \right)^{3/2} P_z \theta. \quad (38)$$

Therefore, a nonzero θ necessarily triggers a nonzero out-of-plane electric polarization, which allows us to identify the θ_{\pm}^* phase with a ferroelectric phase. However, because this phase is only accessible in the presence of externally applied uniaxial strain, we dub it a *piezoelectric* phase. We emphasize that the onset of piezoelectricity is a specific property of D_6 and D_3 lattices only.

The shape of the piezoelectric transition line in the $(\tilde{\varepsilon}, a)$ phase diagram, as well as the character of the transition, can be directly obtained from minimization of Eq. (32). The QTCP takes place for $\mathcal{A} = \mathcal{U} = 0$, yielding

$$a_{\text{QTCP}} = \frac{7}{16}, \quad (39)$$

$$\tilde{\varepsilon}_{\text{QTCP}} = \frac{3}{16}. \quad (40)$$

For $\tilde{\varepsilon} > \tilde{\varepsilon}_{\text{QTCP}}$, the piezoelectric transition is second order since $\mathcal{U} > 0$. In this regime, the transition line is given by $\mathcal{A} = 0$, which corresponds to

$$a_c(\tilde{\varepsilon}) = \frac{2\sqrt{3\tilde{\varepsilon}} - \tilde{\varepsilon}}{3} \quad \text{for } \tilde{\varepsilon} > \tilde{\varepsilon}_{\text{QTCP}}. \quad (41)$$

On the other hand, for $0 < \tilde{\varepsilon} < \tilde{\varepsilon}_{\text{QTCP}}$, $\mathcal{U} < 0$ and the piezoelectric transition is first order. Minimizing Eq. (32), we find that the first-order transition takes place when the following condition is met:

$$\mathcal{A} = \frac{3\mathcal{U}^2}{16\mathcal{W}}, \quad (42)$$

which corresponds to

$$a_c(\tilde{\varepsilon}) = \frac{-1278\tilde{\varepsilon} + 1606\sqrt{3\tilde{\varepsilon}} + \sqrt{15\tilde{\varepsilon}}\sqrt{25344\tilde{\varepsilon} - 12312\sqrt{3\tilde{\varepsilon}} + 4487}}{2214} \quad \text{for } 0 < \tilde{\varepsilon} < \tilde{\varepsilon}_{\text{QTCP}}. \quad (43)$$

Note that this is an approximate expression valid only close to $\tilde{\varepsilon}_{\text{QTCP}}$. In Fig. 4, we show the behavior of different

components of the nematic order parameter, the magnitude ϕ , the projection $\phi_1 = \phi \cos 2\theta$, and the angle θ , as a function

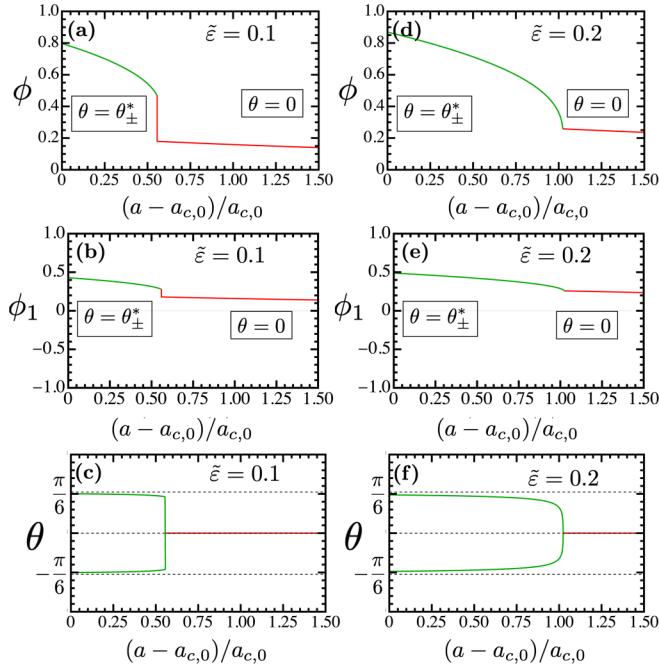


FIG. 4. Behavior of the nematic order parameter for fixed $\tilde{\varepsilon} > 0$ across the first-order transition line [(a)–(c)] and the second-order transition line [(d)–(f)], as defined in the phase diagram of Fig. 2. Representative values of $\tilde{\varepsilon}$ are chosen from the left and right sides of $\tilde{\varepsilon}_{\text{QTCP}} = \frac{3}{16} \approx 0.19$, respectively. The top panels show the magnitude of the nematic order parameter ϕ ; the middle panels show the nematic component projected along the strain direction $\phi_1 = \phi \cos 2\theta$; the bottom panels show the nematic director angle θ . The horizontal axis corresponds to the nonthermal parameter a measured relative to unstrained Potts-nematic transition $a_{c,0} = \frac{2}{9}$. The red curve corresponds to the $\theta = 0$ phase whereas the green curve corresponds to the $\theta = \theta_{\pm}^*$ phase.

of the nonthermal tuning parameter for two different values of $\tilde{\varepsilon} > 0$. For $\tilde{\varepsilon} < \tilde{\varepsilon}_{\text{QTCP}}$, all components change discontinuously across the piezoelectric transition [Figs. 4(a)–4(c)], whereas for $\tilde{\varepsilon} > \tilde{\varepsilon}_{\text{QTCP}}$, all components change continuously [Figs. 4(d)–4(f)]. We note that, for large enough $\tilde{\varepsilon} > 0$, the derivative of the second-order transition line with respect to $\tilde{\varepsilon}$ changes, as described by Eq. (41), resulting in a reentrance of the $\theta_{+} = 0$ phase as a function of strain for fixed a . This behavior is not shown in the phase diagram of Fig. 2 because it only happens for very large strain values $\tilde{\varepsilon} > 3$ (for comparison, recall that the nematic order-parameter jump across the unstrained Potts-nematic transition is $\Delta\phi_0 = \frac{2}{3}$).

We finish this section by discussing the properties of the line of piezoelectric QCPs described by Eq. (41). As in the case of the QCEP discussed in the previous section, the dynamical critical exponent is $z = 1$ in the case of an insulator. For a metallic system, we start from the action (25), substitute $\phi_q = \sqrt{\frac{\tilde{\varepsilon}}{3}}$, and expand for small θ to obtain

$$S_{\text{int}} = \sqrt{\frac{4\tilde{\varepsilon}}{3}} g \int_{k,q} \theta_q \sin(2\tilde{\beta}_{\mathbf{k}}) \psi_{k+q/2}^{\dagger} \psi_{k-q/2}, \quad (44)$$

where, as before, $\tilde{\beta}_{\mathbf{q}} = \beta_{\mathbf{q}} - \alpha$. Note that the electronic dispersion is also renormalized due to the external strain

$\xi_{\mathbf{k}} = \xi_{0,\mathbf{k}} + \sqrt{\frac{\tilde{\varepsilon}}{3}} g \cos(2\tilde{\beta}_{\mathbf{k}})$. Like the QCEP case studied in Sec. II B, the form factor in Eq. (44) is that of an Ising-nematic QCP. Interestingly, the two Ising-nematic form factors in Eqs. (26) and (44) are “orthogonal” in the nematic space, corresponding to the longitudinal and transverse modes of a hypothetical XY nematic order parameter [63,65]. This is a consequence of the fact that, for $\tilde{\varepsilon} < 0$, the nematic director angle is pinned and the nematic amplitude is fluctuating, whereas for $\tilde{\varepsilon} > 0$ it is θ that fluctuates.

To one-loop order, the polarization bubble is given by

$$\Pi(q) = -\frac{8}{3} \tilde{\varepsilon} g^2 \int_k \sin^2(2\tilde{\beta}_{\mathbf{k}}) G_{0,k+q/2} G_{0,k-q/2}, \quad (45)$$

which evaluates to

$$\begin{aligned} \delta\Pi(q) = & -\frac{\tilde{\varepsilon} g^2}{2E_F} f_3\left(\frac{g}{E_F} \sqrt{\frac{\tilde{\varepsilon}}{3}}, \cos 2\tilde{\beta}_{\mathbf{q}}\right) \frac{|\Omega|}{v_F |\mathbf{q}|} \\ & - \frac{\tilde{\varepsilon} g^2}{2E_F} f_4\left(\frac{g}{E_F} \sqrt{\frac{\tilde{\varepsilon}}{3}}, \cos 2\tilde{\beta}_{\mathbf{q}}\right) \left(\frac{\Omega}{v_F |\mathbf{q}|}\right)^2, \end{aligned} \quad (46)$$

where we defined the functions

$$f_3(\tilde{g}, x) = \frac{4}{3\pi} \frac{1 - x^2}{\sqrt{1 - \tilde{g}^2(1 + \tilde{g}x)^{5/2}}}, \quad (47)$$

$$f_4(\tilde{g}, x) = \frac{4}{3\pi} \frac{3\tilde{g}^2 + 4\tilde{g}x + (2 - \tilde{g}^2)(2x^2 - 1)}{(1 - \tilde{g}^2)^{3/2}(1 + \tilde{g}x)^3}. \quad (48)$$

Thus, within a Hertz-Millis approximation for the dynamical critical exponent z , we find $z = 3$, except for the cold spots parametrized by $f_3(x_{\text{cs}}) = 0$, for which $z = 2$. The last result follows from the fact that, since \tilde{g} is small, $f_4(x_{\text{cs}}) > 0$. Moreover, note that $f_3(x) \geq 0$ for any x . Interestingly, in contrast to the QCEP case, here the cold spots are the same as in the case of the undistorted Fermi surface $\tilde{\beta}_{\mathbf{q}} = 0, \pi/2$. This can be understood geometrically by noting that the semimajor axes of the elliptical Fermi surface coincide with its cold spots. As a result, cold-spot fermions at $\beta_{\mathbf{k}} = 0$ ($\beta_{\mathbf{k}} = \pi/2$) will necessarily exchange underdamped collective bosons with momentum direction $\tilde{\beta}_{\mathbf{q}} = \pi/2$ ($\tilde{\beta}_{\mathbf{q}} = 0$).

III. HYSTERESIS AND SPINODAL LINES

The phase boundaries in the phase diagram of Fig. 2 were obtained by determining the global minimum of the action. In the case of first-order transitions, however, the action also has local minima, which correspond to metastable phases. While they are formally inaccessible in true equilibrium, they can be probed via hysteresis measurements in which the order parameter Φ is measured upon cycling the conjugate field $\tilde{\varepsilon}$. The interesting aspect of the Potts-nematic state is that the action has three discrete minima rather than two, which should lead to more complex hysteresis loops as compared to the standard Ising-nematic case.

To calculate these hysteresis curves, we first derive the upper and lower spinodals associated with the first-order transition lines in Fig. 2. As in Sec. II, we consider $\lambda > 0$ and drop the tilde of the rescaled variables (except for $\tilde{\varepsilon}$).

The spinodals are curves on the $(\tilde{\varepsilon}, a)$ plane that bound the regions of metastability of the different phases. We consider first the phase $\theta_- = \pi/2$; it corresponds to a local minimum as long as the following metastability conditions are met:

$$\partial_\phi S_{\text{nem}}(\theta = \pi/2) = \phi^3 - \phi^2 + a\phi + \tilde{\varepsilon} = 0, \quad (49)$$

$$\partial_\phi^2 S_{\text{nem}}(\theta = \pi/2) = 3\phi^2 - 2\phi + a > 0,$$

$$\partial_\theta^2 S_{\text{nem}}(\theta = \pi/2) = 3\phi^3 - \tilde{\varepsilon}\phi > 0. \quad (50)$$

Since $\partial_\theta \partial_\phi S_{\text{nem}}$ vanishes, positive-definiteness of the Hessian matrix of second derivatives $(\partial_i \partial_j S_{\text{nem}})$ is ensured by Eq. (50). It is convenient to define the cubic discriminant of Eq. (49), $\mathcal{D}_{\pi/2} = a^2 - 4a^3 + 4\tilde{\varepsilon} - 27\tilde{\varepsilon}^2 - 18a\tilde{\varepsilon}$. When $\mathcal{D}_{\pi/2} < 0$, Eq. (49) has only one real ϕ solution, whereas when $\mathcal{D}_{\pi/2} > 0$, there are three real ϕ solutions. In the latter case $\mathcal{D}_{\pi/2} > 0$, the largest and smallest values of ϕ that solve Eq. (49) correspond to the two solutions associated with the metanematic transition. On the other hand, in the former case $\mathcal{D}_{\pi/2} < 0$, the single real solution indicates that there is no metanematic transition, as is the case to the left of the QCEP. This suggests that $\mathcal{D}_{\pi/2} = 0$ gives the spinodals associated with the metanematic transition. There is, however, one subtlety: by construction, ϕ must be positive. Therefore, it is not enough to ensure the existence of a real solution, but of a real and positive solution. It turns out that, when $\tilde{\varepsilon} < 0$, the real solutions of Eq. (49) in both cases ($\mathcal{D}_{\pi/2} > 0$ and $\mathcal{D}_{\pi/2} < 0$) are always positive. However, when $\tilde{\varepsilon} > 0$, the single solution in the $\mathcal{D}_{\pi/2} < 0$ case is negative, whereas only one among the two positive solutions in the $\mathcal{D}_{\pi/2} > 0$ case is an action minimum. Taking these conditions into account and solving the equation $\mathcal{D}_{\pi/2} = 0$ for a , we find the equations describing the spinodals of the metanematic transition. The three solutions of $\mathcal{D}_{\pi/2} = 0$ can be written as

$$a_n(\tilde{\varepsilon}) = \frac{1}{12} \left(1 - e^{2n\pi/3} b(\tilde{\varepsilon}) + e^{-2n\pi/3} \frac{216\tilde{\varepsilon} - 1}{b(\tilde{\varepsilon})} \right), \quad (51)$$

$$b(\tilde{\varepsilon}) = [108\tilde{\varepsilon}(54\tilde{\varepsilon} - 5) + 24\sqrt{3\tilde{\varepsilon}(27\tilde{\varepsilon} + 1)^3} - 1]^{1/3} \quad (52)$$

with $n = 0, 1, 2$. Then, the upper spinodal is given by

$$a_{\text{us}}^{\text{meta}}(\tilde{\varepsilon}) = \begin{cases} a_1(\tilde{\varepsilon}), & \text{for } \tilde{\varepsilon}_{\text{QCEP}} < \tilde{\varepsilon} < \tilde{\varepsilon}_* \\ a_0(\tilde{\varepsilon}), & \text{for } \tilde{\varepsilon} > \tilde{\varepsilon}_* \end{cases} \quad (53)$$

with $\tilde{\varepsilon}_* = \frac{1}{216}$ defined such that $b(\tilde{\varepsilon}_*) = 0$. For the lower spinodal, we obtain

$$a_{\text{ls}}^{\text{meta}}(\tilde{\varepsilon}) = a_2(\tilde{\varepsilon}), \quad \text{for } \tilde{\varepsilon}_{\text{QCEP}} < \tilde{\varepsilon} < 0.$$

Here, the subscripts ‘‘us’’ and ‘‘ls’’ denote upper spinodal and lower spinodal, respectively. In particular, $a_{\text{us}}^{\text{meta}}(\tilde{\varepsilon})$ gives the limit of metastability of the θ_- phase below the metanematic transition line, whereas $a_{\text{ls}}^{\text{meta}}(\tilde{\varepsilon})$ gives the limit of metastability of the θ_- phase above the metanematic transition line. These spinodal lines are shown by the blue dashed lines in the phase diagram of Fig. 5.

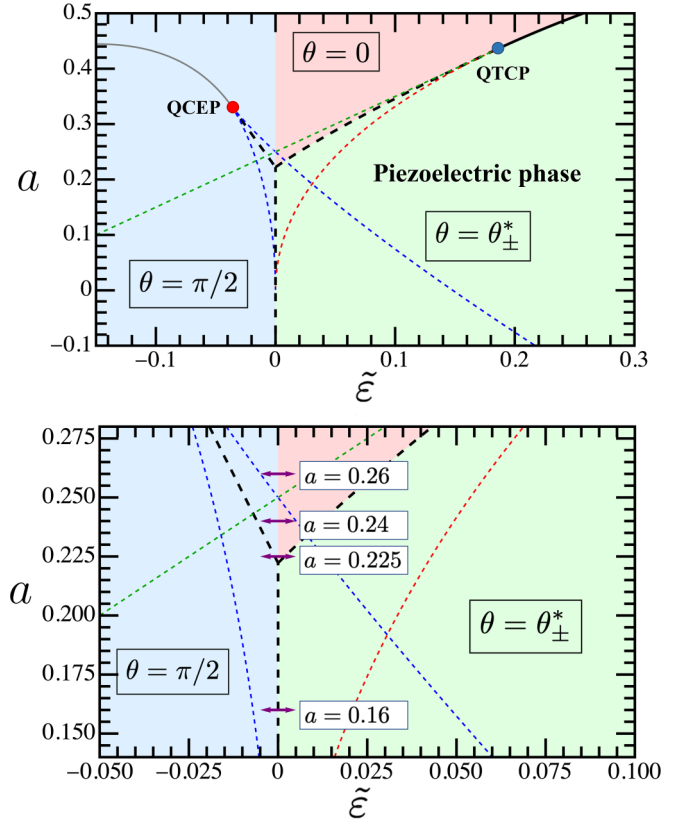


FIG. 5. The zero-temperature phase diagram of Fig. 2 is shown with the spinodal lines included (top panel). The two blue dashed lines on the left side ($\tilde{\varepsilon} < 0$) are the upper and lower spinodals corresponding to the two phases associated with the metanematic transition. They coincide at the QCEP. The green and red dashed curves on the right side ($\tilde{\varepsilon} > 0$) are the upper and lower spinodals of the $\theta = \theta_\pm^*$ (piezoelectric) and $\theta = 0$ phases, respectively. They coincide at the QTCP. The bottom panel is a zoom of the top panel; the purple arrows show the values of a for which the hysteresis curves $\Phi(\tilde{\varepsilon})$ in Fig. 6 are shown.

We now analyze the metastability of the $\theta_+ = 0$ phase. The metastability conditions are given by

$$\partial_\phi S_{\text{nem}}(\theta = 0) = \phi^3 + \phi^2 + a\phi - \tilde{\varepsilon} = 0, \quad (54)$$

$$\partial_\phi^2 S_{\text{nem}}(\theta = 0) = 3\phi^2 + 2\phi + a > 0,$$

$$\partial_\theta^2 S_{\text{nem}}(\theta = 0) = -3\phi^3 + \tilde{\varepsilon}\phi > 0. \quad (55)$$

Applying a similar analysis as in the $\theta_- = \pi/2$ case, we find that $\theta_+ = 0$ ceases to be a local minimum when the second condition of Eq. (55) fails. Plugging in $\phi^2 = \tilde{\varepsilon}/3$ into Eq. (54), we find

$$a_{\text{ls}}^{\text{piezo}}(\tilde{\varepsilon}) = \frac{2\sqrt{3\tilde{\varepsilon}} - \tilde{\varepsilon}}{3}, \quad \text{for } 0 < \tilde{\varepsilon} < \tilde{\varepsilon}_{\text{QTCP}} \quad (56)$$

which corresponds to the lower spinodal of the first-order piezoelectric phase transition, shown by the dashed red line in the phase diagram of Fig. 5. To obtain the upper spinodal of this transition, we need to analyze the metastability of the $\theta = \theta_\pm^*$ phase. Equation (3) gives the nematic magnitude ϕ_\pm^* in the θ_\pm^* phase. For $\tilde{\varepsilon} < \tilde{\varepsilon}_{\text{QTCP}}$, the condition $(\phi_\pm^*)^2 \geq \tilde{\varepsilon}/3$ required for θ_\pm^* in Eq. (12) to exist is always satisfied.

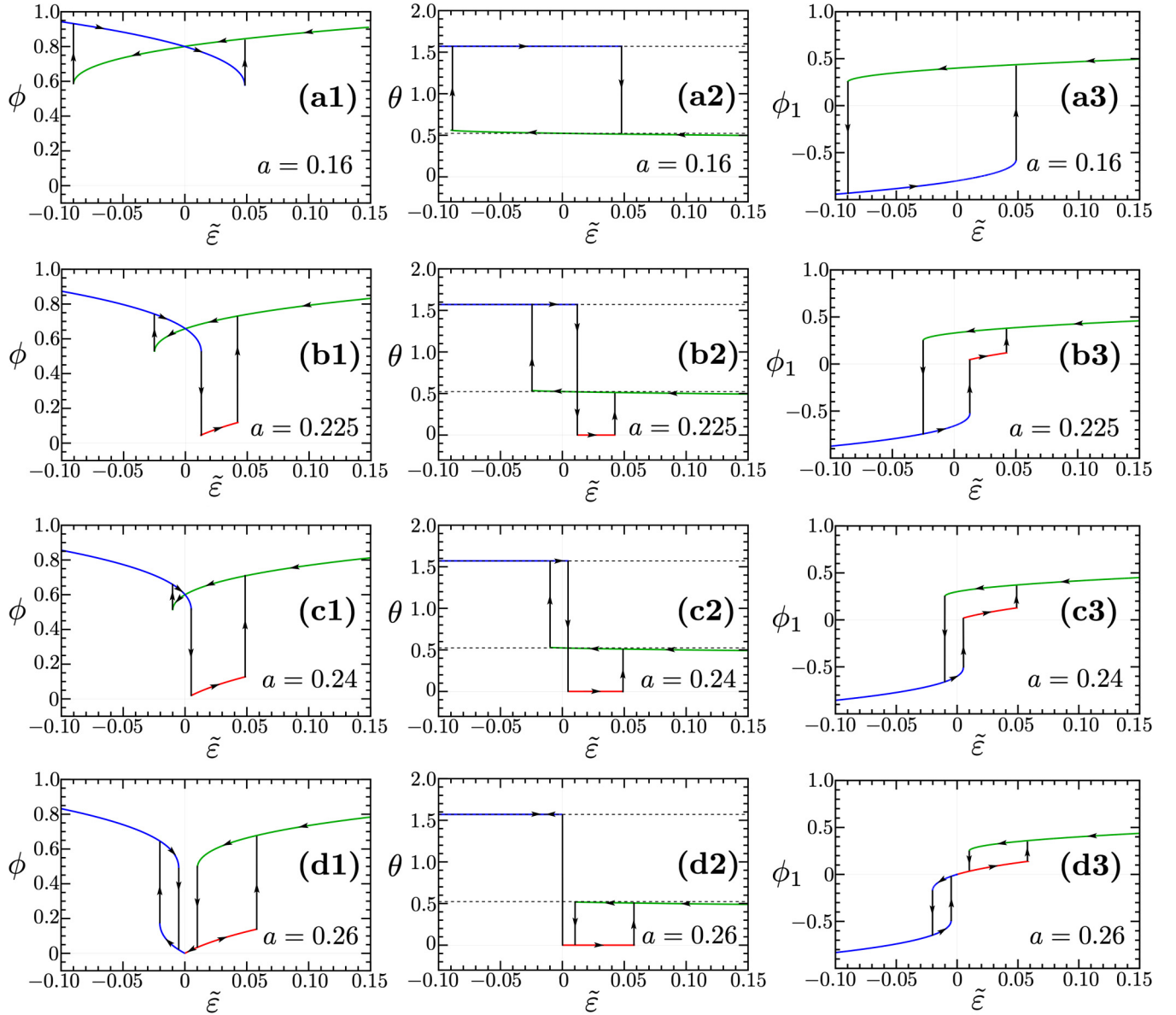


FIG. 6. Hysteresis curves of the nematic order parameter as a function of uniaxial strain $\tilde{\varepsilon}$ for four representative values of a marked by the purple arrows in Fig. 5. (a) Corresponds to $a = 0.16$; (b) to $a = 0.225$; (c) to $a = 0.24$; and (d) to $a = 0.26$. Left, middle, and right panels, which are identified by the numbers 1, 2, and 3, respectively, correspond to the nematic magnitude ϕ , the nematic director angle θ , and the nematic component projected along the direction of the strain $\phi_1 = \phi \cos 2\theta$. Red, green, and blue colors denote the action minimum $\theta = 0$, $\theta = \theta_+^*$, and $\theta = \pi/2$, respectively.

Moreover, the ϕ_+^* solution exists as long as the argument of the square root in Eq. (3) is positive, $a < \tilde{\varepsilon} + \frac{1}{4}$. This therefore defines the limit of metastability of the θ_{\pm}^* phase, which corresponds to the upper spinodal of the first-order piezoelectric transition. It is shown by the dashed green line in Fig. 5(a) and given by

$$a_{\text{us}}^{\text{piezo}}(\tilde{\varepsilon}) = \tilde{\varepsilon} + \frac{1}{4}, \quad \text{for } \tilde{\varepsilon} < \tilde{\varepsilon}_{\text{QTCP}} \quad (57)$$

Interestingly, for $\tilde{\varepsilon} > \tilde{\varepsilon}_{\text{QTCP}}$, the condition $(\phi_+^*)^2 \geq \tilde{\varepsilon}/3$ would imply an upper spinodal $a_{\text{us}}^{\text{piezo}}(\tilde{\varepsilon}) = \frac{2\sqrt{3\tilde{\varepsilon}-\tilde{\varepsilon}}}{3}$, which is identical to what the lower spinodal would be in this strain range [see Eq. (56)]. The coincidence between the upper and

lower spinodals implies that the transition is actually second order. Indeed, these would-be spinodals have the same expression as the one describing the second-order transition line, Eq. (41).

We are now in position to analyze the hysteresis curves $\Phi(\tilde{\varepsilon})$ as the strain $\tilde{\varepsilon}$ is cycled. We employ the Stoner-Wohlfarth approach [70]: starting deep in one of the ordered states, we assume that the system remains in this state until it is no longer a local minimum of the action, i.e., until its spinodal line is crossed, at which point the system moves to another minimum. In the Ising-nematic case, this last step is straightforward, as there is only one minimum available in the action landscape after the spinodal line is crossed. However,

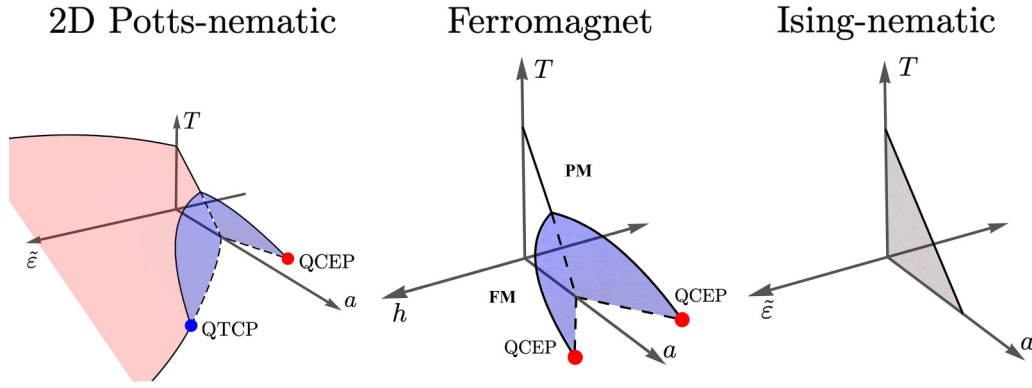


FIG. 7. Left panel: Qualitative $(\bar{\varepsilon}, a, T)$ phase diagram of a 2D Potts-nematic system (same as Fig. 1). Middle panel: (h, a, T) phase diagram of an itinerant ferromagnet, where h is the magnetic field (see Refs. [71,72]). The first-order wings are symmetric with respect to h and are bounded by a line of classical critical end points terminating at QCEPs. Right panel: $(\bar{\varepsilon}, a, T)$ phase diagram of an Ising-nematic system. There is a second-order transition only along the $\bar{\varepsilon} = 0$ plane. Any nonzero strain along the nematic director directions smears the transition completely.

in the Potts-nematic case, there can be two local minima. To decide which of the two minima the system chooses, we employ a “gradient-descent criterion.” Specifically, we introduce a “time” variable s , promoting Φ to a dynamical field $\Phi(s)$, and define a generalized gradient-descent equation

$$\dot{\phi}_i = -\eta_{ij} \frac{\partial S_{\text{nem}}}{\partial \phi_j}, \quad (58)$$

where, we recall, $\Phi \equiv (\phi_1, \phi_2) = \phi(\cos 2\theta, \sin 2\theta)$. Here, repeated indices are implicitly summed, $\dot{\phi}_i = \partial \phi_i / \partial s$, and η_{ij} is a positive-definite matrix. The last condition ensures that Eq. (58) remains purely diffusive, such that Φ approaches a local minimum of S_{nem} as $s \rightarrow \infty$. We set $\eta_{ij} = \eta \delta_{ij}$ with $\eta > 0$, in which case solutions to Eq. (58) are trajectories of steepest descent. We rescale $s \rightarrow s' = s/\eta$ and redefine $\dot{\phi}_i = \partial \phi_i / \partial s'$ to obtain the autonomous system

$$\begin{aligned} \dot{\phi}_1 &= -a\phi_1 - \phi_1(\phi_1^2 + \phi_2^2) - (\phi_1^2 - \phi_2^2) + \bar{\varepsilon}, \\ \dot{\phi}_2 &= -a\phi_2 - \phi_2(\phi_1^2 + \phi_2^2) + 2\phi_1\phi_2. \end{aligned} \quad (59)$$

The procedure we adopt once the system approaches a spinodal at $\bar{\varepsilon}^*$, for a fixed a value, is as follows: let $\bar{\varepsilon}^+$ and $\bar{\varepsilon}^-$ be strain values near $\bar{\varepsilon}^*$ and within the unstable and stable sides of the spinodal curve, respectively. Let $\Phi_{\text{min}}^{(\bar{\varepsilon}^-)}$ be the local minimum of the action at $\bar{\varepsilon} = \bar{\varepsilon}^-$, which disappears once $\bar{\varepsilon} = \bar{\varepsilon}^+$. We then set $\bar{\varepsilon} = \bar{\varepsilon}^+$ in Eq. (59) and choose several initial conditions $\Phi(0)$ in a narrow neighborhood of $\Phi_{\text{min}}^{(\bar{\varepsilon}^-)}$, $|\Phi(0) - \Phi_{\text{min}}^{(\bar{\varepsilon}^-)}| \lesssim 10^{-4}$, letting the system evolve until a new local minima is encountered. We found that $\Phi(s)$ approaches the same minimum for all initial conditions we investigated, which suggests that the outcome is insensitive to any initial condition within a small vicinity of $\Phi_{\text{min}}^{(\bar{\varepsilon}^-)}$.

We applied this procedure to four representative fixed values of a in the phase diagram of Fig. 5, marked by the purple arrows in the bottom panel. They each correspond to one of the four regions bounded by the values of a in which two

different spinodal lines intersect, namely,

$$\begin{aligned} a_1 &= -39 + 16\sqrt{6} \approx 0.1918, \\ a_2 &= \frac{-45 + 13\sqrt{13}}{8} \approx 0.2340, \\ a_3 &= a_{\text{us}}^{\text{Potts}} = 0.25. \end{aligned} \quad (60)$$

Here, a_1 corresponds to the crossing between the blue and red dashed spinodal lines; a_2 corresponds to the lower crossing between the blue and green dashed spinodal lines; and a_3 corresponds to the upper crossing between the blue and green dashed spinodal lines, which also coincides with the upper spinodal of the unstrained Potts transition.

The hysteresis curves for the four representative a values marked in Fig. 5 are shown in Fig. 6. In this figure, we present the hysteresis curves for the nematic magnitude $\phi(\bar{\varepsilon})$, the nematic director angle $\theta(\bar{\varepsilon})$, and the nematic component projected along the strain direction $\phi_1 = \phi \cos 2\theta$. Figures 6(a1)–6(a3) show the case $a = 0.16 < a_1$. The system starts deep inside the θ_{\pm}^* green phase (piezoelectric phase) when $\bar{\varepsilon}$ is large and positive. Upon decreasing $\bar{\varepsilon}$ (from right to left in Figs. 6(a1)–6(a3)), the system remains in the metastable θ_{\pm}^* phase until it reaches the dashed green spinodal line, where $\bar{\varepsilon} < 0$. At this point, the only available minimum is the $\theta_- = \pi/2$ blue phase below the metanematic transition. Once we reverse $\bar{\varepsilon}$ and start increasing it [from left to right in Figs. 6(a1)–6(a3)], the system remains in the $\theta_- = \pi/2$ phase until the spinodal blue dashed line is crossed in the $\bar{\varepsilon} > 0$ side of the phase diagram, at which point the system moves back to the θ_{\pm}^* green phase. In terms of the ϕ_1 component, the hysteresis curve is a rather standard one, albeit not symmetric with respect to either the ϕ_1 or the $\bar{\varepsilon}$ axes.

Figures 6(b1)–6(b3) show the hysteresis curves for the case $a_1 < a = 0.225 < a_2$. Starting deep from the $\bar{\varepsilon} > 0$ side of the phase diagram and then decreasing $\bar{\varepsilon}$ (i.e., going from right to left in the plots), the situation is the same as in Figs. 6(a1)–6(a3), namely, the system remains in the θ_{\pm}^* green phase until the green spinodal line is crossed on the $\bar{\varepsilon} < 0$ side of the phase diagram. However, upon reversing $\bar{\varepsilon}$ and increasing it (i.e., going from left to right in the plots), the

situation changes. Once the blue dashed spinodal line is crossed, on the $\tilde{\varepsilon} > 0$ side of the phase diagram, there are two local minima available: the global minimum corresponding to the θ_{\pm}^* green phase and the metastable minimum corresponding to the $\theta_{+} = 0$ red phase. By solving Eq. (58), we find that the system moves to the $\theta_{+} = 0$ red phase and remains at this local minimum until the red dashed spinodal line is crossed, at which point the system finally moves back to the θ_{\pm}^* green phase. This behavior results in multiloop hysteresis curves.

The case $a_2 < a = 0.24 < a_3$ is depicted in Figs. 6(c1)–6(c3). The behavior upon increasing $\tilde{\varepsilon}$ (i.e., going from left to right in the plots) is the same as in Figs. 6(b1)–6(b3). On the other hand, the sequence of spinodals crossed upon decreasing $\tilde{\varepsilon}$ (i.e., going from right to left in the plots) is different: once the green dashed spinodal line is crossed, there are now two local minima available, corresponding to the two $\theta_{-} = \pi/2$ blue phases associated with the two sides of the metanematic transition. The solution of Eq. (58) shows that the system moves to the global minimum, where it remains as $\tilde{\varepsilon}$ continues being decreased. Therefore, although the sequence of spinodals crossed is different from the case of Figs. 6(b1)–6(b3), the sequence of metastable phases probed is the same.

Finally, Figs. 6(d1)–6(d3) show the case $a = 0.26 > a_3$. Upon decreasing $\tilde{\varepsilon}$ (right to left in the plots), the green dashed spinodal line is now crossed on the $\tilde{\varepsilon} > 0$ side of the phase diagram. The only available minimum is the $\theta_{+} = 0$ phase, which however ceases to be a solution once the $\tilde{\varepsilon} = 0$ line is crossed. At this axis, $\phi \rightarrow 0$, which is a consequence of the fact that the system is above the upper spinodal a_3 of the unstrained Potts-nematic transition. The system then moves to the $\theta_{-} = \pi/2$ blue phase above the metanematic transition, where it remains until the lower blue dashed spinodal line is crossed. At this point, the system moves to the $\theta_{-} = \pi/2$ blue phase below the metanematic transition. The behavior upon increasing $\tilde{\varepsilon}$ (left to right in the plots) can be understood in a similar manner. The resulting hysteresis curves display multiple loops which, however, do not cross the origin since $\phi = 0$ when $\tilde{\varepsilon} = 0$.

IV. NONZERO-TEMPERATURE PHASE DIAGRAM

At $T = 0$, the Potts-nematic phase diagram is expected to be the same for both 2D and 3D systems since in either case the effective dimensionality $d + z$ is larger than the upper critical dimension of the 3-state Potts model $d_u^{\text{Potts}} \lesssim 3$, such that a mean-field analysis is warranted. At larger temperatures, where the bosonic quantum dynamics can be neglected, the situation is different. Since $d = 3 > d_u^{\text{Potts}}$, in the 3D case the $(\tilde{\varepsilon}, a, T)$ phase diagram consists essentially of a sequence of “copies” of the phase diagram shown in Fig. 2. Similarly, for a fixed a , the $(\tilde{\varepsilon}, T)$ phase diagram has the same form as the one obtained at $T = 0$, but with the y axis representing $T - T_c$.

The situation at nonzero temperatures is more interesting in the 2D case. The fact that $d = 2 < d_u^{\text{Potts}}$ implies that the mean-field solution is not applicable. Surprisingly, despite the presence of a cubic invariant in the free-energy expansion, the 2D 3-state Potts model undergoes a second-order transition characterized by the critical exponents $\alpha = \frac{1}{3}$ and $\beta = \frac{1}{9}$, which are in the universality class of the hard hexagon lattice gas model [61]. Of course, one cannot exclude the possibility

that for particular microscopic models the quartic Landau coefficient is negative, rendering the transition first order. But, in the general case, we expect that, in the absence of strain and at high enough temperatures, the Potts-nematic transition is second order. As a result, since at $T = 0$ the Potts-nematic transition is first order, the (a, T) phase diagram with fixed $\tilde{\varepsilon} = 0$ should display a (classical) tricritical point. It is difficult to estimate the position of this tricritical point since standard perturbative approaches such as renormalization-group calculations do not capture the second-order character of the transition in 2D. It would be interesting to perform Monte Carlo simulations to pinpoint the position of the classical tricritical point.

Having established the $(\tilde{\varepsilon}, a)$ phase diagram at $T = 0$ and the (a, T) phase diagram at $\tilde{\varepsilon} = 0$, we can conjecture the full qualitative three-dimensional $(\tilde{\varepsilon}, a, T)$ phase diagram for the 2D Potts-nematic model by continuously connecting the QTCP and the QCEP at $T = 0$ with the classical tricritical point at $\tilde{\varepsilon} = 0$. The result, shown in Fig. 1 and repeated for convenience in the left panel of Fig. 7, consists of two wings (in blue) inside which the transition is first order. On the $\tilde{\varepsilon} < 0$ side, the wing is isolated and the transition is a symmetry-preserving metanematic one. On the other hand, on the $\tilde{\varepsilon} > 0$ side, the wing is connected to a larger surface (in red) that signals a second-order transition. Regardless of the character of the transition in the $\tilde{\varepsilon} > 0$ region, it is associated with the spontaneous breaking of an in-plane twofold rotational symmetry, which is manifested as a piezoelectric phase in the case of twisted moiré systems.

It is interesting to compare this $(\tilde{\varepsilon}, a, T)$ phase diagram with that expected for an Ising-nematic order parameter, as realized in tetragonal lattices. As shown in the right panel of Fig. 7, in the Ising-nematic case the system is generically expected to undergo a second-order transition only along the $\tilde{\varepsilon} = 0$ plane. Any strain applied along the directions of the nematic director completely smears the Ising-nematic phase transition. This is what renders it difficult to unambiguously distinguish spontaneous Ising-nematic order from strain-induced anisotropies in experimental settings, where residual strain is invariably present. In contrast, metanematic and piezoelectric transitions persist for a wide range of strain values in the case of Potts-nematic order. Experimental observation of these effects would provide direct evidence for spontaneous Potts-nematic order.

The wings in the $(\tilde{\varepsilon}, a, T)$ phase diagram of the Potts-nematic order, bounded by tricritical points and critical end points, are reminiscent of the wings generally expected in the (h, a, T) phase diagram of a metallic (Heisenberg) ferromagnet, which is schematically shown in the middle panel of Fig. 7 (see Refs. [71,72]). Note that here h denotes a magnetic field. At first sight, this analogy may seem unsurprising since both $\tilde{\varepsilon}$ and h act as conjugate fields to the nematic and ferromagnetic order parameters, respectively. However, there are crucial qualitative differences. First, because the nematic order parameter is 3-state Potts-type rather than continuous, there is a fundamental asymmetry between the effects of compressive strain and tensile strain, whereas in the ferromagnetic case the phase diagram is symmetric with respect to the sign of the magnetic field. Second, the mechanisms behind the first-order $T = 0$ transitions are completely different in the

two cases. In the Potts-nematic case, the first-order nature of the quantum phase transition is an intrinsic property of the bosonic model, as it is a direct consequence of it being above its upper critical dimension. In contrast, in the metallic ferromagnetic case, the $T = 0$ transition is rendered first order due to the coupling between the ferromagnetic Goldstone modes and the gapless electron-hole excitations of the metal [73–75].

V. CONCLUSIONS

In this paper, we used a phenomenological approach to establish the $(\tilde{\epsilon}, a, T)$ phase diagram of the electronic 3-state Potts-nematic model in the presence of uniaxial strain applied along one of the high-symmetry directions of a lattice that possesses out-of-plane threefold rotational symmetry and in-plane twofold rotational symmetry. While a is a nonthermal tuning parameter, such as doping, the parameter $\tilde{\epsilon}$ is linearly proportional to the applied strain. Whether compressive or tensile strain gives $\tilde{\epsilon} < 0$ or $\tilde{\epsilon} > 0$ depends on the signs of the cubic nematic coefficient and the nematoelastic coupling. At zero temperature and zero strain, the mean-field approach is justified due to the reduced upper critical dimension of the 3-state Potts model $d_u^{\text{Potts}} \lesssim 3$. Then, because the Potts-nematic action contains a cubic invariant, there is no Potts-nematic QCP, but rather a first-order Potts-nematic quantum phase transition. Upon increasing the temperature, but keeping the strain zero, the mean-field solution ceases to be valid in the case of a 2D lattice, and the Potts-nematic transition becomes second order. Thus, a classical tricritical nematic point is generally expected in an unstrained 2D system, whereas in a 3D system the Potts-nematic transition should be always first order.

Notwithstanding the absence of a QCP in an unstrained 2D or 3D system, application of strain can tune the system across a metanematic QCEP, for $\tilde{\epsilon} < 0$, and a QTCP followed by a line of QCPs for $\tilde{\epsilon} > 0$. The former transition is symmetry preserving, whereas the latter spontaneously breaks the in-plane twofold rotational symmetry of the lattice. Note that a nonzero $\tilde{\epsilon}$ explicitly breaks the out-of-plane threefold rotational symmetry. In lattices with D_3 and D_6 point-group symmetries, which is the case for instance of twisted bilayer graphene (TBG) and twisted double-bilayer graphene (TDBG), the transition in the $\tilde{\epsilon} > 0$ side of the phase diagram leads to the emergence of a nonzero electric polarization, resulting in what we dubbed a piezoelectric phase, since the ferroelectric order requires the presence of external strain. Connecting the phase diagrams at zero strain and at zero temperature, we proposed the $(\tilde{\epsilon}, a, T)$ phase diagram for a 2D Potts-nematic system shown in Fig. 1. One of its key features is the existence of two first-order transition wings, bounded by a line of tricritical points in the $\tilde{\epsilon} > 0$ side of the phase diagram, and by a line of critical end points in the $\tilde{\epsilon} < 0$ side. While the latter wing is isolated, the former is connected to an open surface of second-order phase transitions towards the piezoelectric phase. The recent observation of electronic nematicity in TBG [26–29], TDBG [30], and twisted trilayer graphene [31], which are 2D materials, indicate not only that the phase diagram of Fig. 1 may be realized in moiré superlattices, but also that strain can be used to move the system towards nematic quantum criticality.

Note that this is a different mechanism from that proposed in Ref. [82] to strain tune TBG across a quantum phase transition.

It is interesting to contrast the results obtained here for the Potts-nematic phase with those for an Ising-nematic phase, which is realized in lattices with fourfold rotational symmetry. In the Ising-nematic case, “longitudinal” strain applied along either of the two allowed nematic director directions smears the second-order phase transition. However, “transverse” strain applied along the other two high-symmetry directions not encompassed by the nematic director can tune the system towards an Ising-nematic QCP [83]. This offers an interesting insight into why strain is capable of tuning the system across a Potts-nematic QCP. For the lattices considered here, the nematic director can point along any of the high-symmetry lattice directions. Thus, uniaxial strain applied along these directions can have either a “longitudinal” or a “transverse” character, depending on whether strain is compressive or tensile. This asymmetry between compressive and tensile strain traces back to the well-understood inequivalence between positive and negative conjugate fields in the mean-field solution of the 3-state Potts model [59,60].

The Potts-nematic QCPs that emerge in the presence of strain behave analogously to an Ising-nematic QCP in the absence of strain. In both the $\tilde{\epsilon} > 0$ and $\tilde{\epsilon} < 0$ sides of the phase diagram, the two-component Potts-nematic order parameter is effectively reduced to a single-component one by the external strain, either because the nematic amplitude jumps between two nonzero values while the nematic director angle is pinned by the strain ($\tilde{\epsilon} < 0$), or because the nematic director unlocks from the strain direction by rotating along the clockwise or the counterclockwise direction ($\tilde{\epsilon} > 0$). In fact, under these conditions, the Potts-nematic electronic form factor reduces to the well-known “ B_{1g} ” Ising-nematic form factor for $\tilde{\epsilon} < 0$ and “ B_{2g} ” Ising-nematic form factor for $\tilde{\epsilon} > 0$. Consequently, while the QCPs on the two sides of the phase diagram have the same Hertz-Millis dynamical critical exponent $z = 3$ except for a few cold spots, for which $z = 2$, these cold spots are at different locations depending on the sign of $\tilde{\epsilon}$. More broadly, the strain-induced Potts-nematic QCPs should support the same phenomena expected for the Ising-nematic QCP, such as superconductivity and non-Fermi-liquid behavior [66–68,84–86].

Our results provide valuable criteria to experimentally identify intrinsic Potts-nematic order and distinguish it from extrinsic effects via a controlled application of uniaxial strain. Observation of the characteristic multiloop hysteresis curves shown in Fig. 6 would be a direct confirmation not only of long-range nematic order, but also of the Potts-type character of the order parameter. Experimentally, ϕ_1 can be probed via resistivity anisotropy measurements similarly to those carried out in the pnictides [8]. In this regard, as pointed out in Ref. [87], the geometry used to measure the resistivity plays an important role in extracting the anisotropic component of the resistivity tensor (see also Ref. [16]). Moreover, the observation of a piezoelectric effect in twisted moiré systems that only emerges for one type of strain (compressive or tensile) would provide unambiguous evidence for an intrinsic Potts-nematic instability. Interestingly, ferroelectricity has been recently observed in a moiré heterostructure [88]. While

in this paper we focused only on externally applied uniform strain, any crystalline system will invariably be subjected to internal random strain [13–15]. Given the nontrivial impact of uniform strain on the Potts nematicity, it will be interesting for future studies to shed light on the properties of the 3-state Potts-nematic model in the presence of both random strain and uniform strain. The random-field Potts model is believed to behave similarly to the random-field Ising model, in that long-range order is robust against weak random-field disorder in $d = 3$ but cannot be established in $d = 2$ [89]. Nevertheless, as discussed in Ref. [90], the relatively small

number of moiré unit cells present in realistic twisted moiré devices could protect nematic order against domain breakup.

ACKNOWLEDGMENTS

We thank H. Ochoa and J. Venderbos for fruitful discussions. This work was supported by the U. S. Department of Energy, Office of Science, Basic Energy Sciences, Materials Sciences and Engineering Division, under Award No. DE-SC0020045.

-
- [1] S. A. Kivelson, E. Fradkin, and V. J. Emery, *Nature (London)* **393**, 550 (1998).
- [2] S. A. Kivelson, I. P. Bindloss, E. Fradkin, V. Oganesyan, J. M. Tranquada, A. Kapitulnik, and C. Howald, *Rev. Mod. Phys.* **75**, 1201 (2003).
- [3] V. Hinkov, D. Haug, B. Fauqué, P. Bourges, Y. Sidis, A. Ivanov, C. Bernhard, C. Lin, and B. Keimer, *Science* **319**, 597 (2008).
- [4] M. Vojta, *Adv. Phys.* **58**, 699 (2009).
- [5] R. Okazaki, T. Shibauchi, H. Shi, Y. Haga, T. Matsuda, E. Yamamoto, Y. Onuki, H. Ikeda, and Y. Matsuda, *Science* **331**, 439 (2011).
- [6] F. Ronning, T. Helm, K. Shirer, M. Bachmann, L. Balicas, M. K. Chan, B. Ramshaw, R. D. McDonald, F. F. Balakirev, M. Jaime *et al.*, *Nature (London)* **548**, 313 (2017).
- [7] S. Seo, X. Wang, S. M. Thomas, M. C. Rahn, D. Carmo, F. Ronning, E. D. Bauer, R. D. dos Reis, M. Janoschek, J. D. Thompson, R. M. Fernandes, and P. F. S. Rosa, *Phys. Rev. X* **10**, 011035 (2020).
- [8] J.-H. Chu, H.-H. Kuo, J. G. Analytis, and I. R. Fisher, *Science* **337**, 710 (2012).
- [9] R. Fernandes, A. Chubukov, and J. Schmalian, *Nat. Phys.* **10**, 97 (2014).
- [10] A. E. Böhmer and C. Meingast, *C. R. Phys.* **17**, 90 (2016).
- [11] A. E. Böhmer, J.-H. Chu, S. Lederer, and M. Yi, *Nat. Phys.* **18**, 1412 (2022).
- [12] E. Fradkin, S. A. Kivelson, M. J. Lawler, J. P. Eisenstein, and A. P. Mackenzie, *Annu. Rev. Condens. Matter Phys.* **1**, 153 (2010).
- [13] E. W. Carlson, K. A. Dahmen, E. Fradkin, and S. A. Kivelson, *Phys. Rev. Lett.* **96**, 097003 (2006).
- [14] E. Carlson and K. Dahmen, *Nat. Commun.* **2**, 379 (2011).
- [15] W. J. Meese, T. Vojta, and R. M. Fernandes, *Phys. Rev. B* **106**, 115134 (2022).
- [16] X. Wang, J. Finney, A. L. Sharpe, L. K. Rodenbach, C. L. Hsueh, K. Watanabe, T. Taniguchi, M. Kastner, O. Vafek, and D. Goldhaber-Gordon, [arXiv:2209.08204](https://arxiv.org/abs/2209.08204).
- [17] U. Karahasanovic and J. Schmalian, *Phys. Rev. B* **93**, 064520 (2016).
- [18] I. Paul and M. Garst, *Phys. Rev. Lett.* **118**, 227601 (2017).
- [19] V. S. de Carvalho and R. M. Fernandes, *Phys. Rev. B* **100**, 115103 (2019).
- [20] P. Massat, J. Wen, J. M. Jiang, A. T. Hristov, Y. Liu, R. W. Smaha, R. S. Feigelson, Y. S. Lee, R. M. Fernandes, and I. R. Fisher, *Proc. Natl. Acad. Sci. USA* **119**, e2119942119 (2022).
- [21] B. E. Feldman, M. T. Randeria, A. Gyenis, F. Wu, H. Ji, R. J. Cava, A. H. MacDonald, and A. Yazdani, *Science* **354**, 316 (2016).
- [22] Y. Sun, S. Kittaka, T. Sakakibara, K. Machida, J. Wang, J. Wen, X. Xing, Z. Shi, and T. Tamegai, *Phys. Rev. Lett.* **123**, 027002 (2019).
- [23] C.-w. Cho, J. Shen, J. Lyu, O. Atanov, Q. Chen, S. H. Lee, Y. S. Hor, D. J. Gawryluk, E. Pomjakushina, M. Bartkowiak *et al.*, *Nat. Commun.* **11**, 3056 (2020).
- [24] A. Little, C. Lee, C. John, S. Doyle, E. Maniv, N. L. Nair, W. Chen, D. Rees, J. W. Venderbos, R. M. Fernandes *et al.*, *Nat. Mater.* **19**, 1062 (2020).
- [25] S. Jin, W. Zhang, X. Guo, X. Chen, X. Zhou, and X. Li, *Phys. Rev. Lett.* **126**, 035301 (2021).
- [26] A. Kerelsky, L. J. McGilly, D. M. Kennes, L. Xian, M. Yankowitz, S. Chen, K. Watanabe, T. Taniguchi, J. Hone, C. Dean *et al.*, *Nature (London)* **572**, 95 (2019).
- [27] Y. Jiang, X. Lai, K. Watanabe, T. Taniguchi, K. Haule, J. Mao, and E. Y. Andrei, *Nature (London)* **573**, 91 (2019).
- [28] Y. Choi, J. Kemmer, Y. Peng, A. Thomson, H. Arora, R. Polski, Y. Zhang, H. Ren, J. Alicea, G. Refael *et al.*, *Nat. Phys.* **15**, 1174 (2019).
- [29] Y. Cao, D. Rodan-Legrain, J. M. Park, N. F. Yuan, K. Watanabe, T. Taniguchi, R. M. Fernandes, L. Fu, and P. Jarillo-Herrero, *Science* **372**, 264 (2021).
- [30] C. Rubio-Verdú, S. Turkel, Y. Song, L. Klebl, R. Samajdar, M. S. Scheurer, J. W. Venderbos, K. Watanabe, T. Taniguchi, H. Ochoa *et al.*, *Nat. Phys.* **18**, 196 (2022).
- [31] N. J. Zhang, Y. Wang, K. Watanabe, T. Taniguchi, O. Vafek, and J. Li, [arXiv:2211.01352](https://arxiv.org/abs/2211.01352).
- [32] C. Jin, Z. Tao, T. Li, Y. Xu, Y. Tang, J. Zhu, S. Liu, K. Watanabe, T. Taniguchi, J. C. Hone *et al.*, *Nat. Mater.* **20**, 940 (2021).
- [33] A. Mulder, R. Ganesh, L. Capriotti, and A. Paramekanti, *Phys. Rev. B* **81**, 214419 (2010).
- [34] V. Drouin-Touchette, P. P. Orth, P. Coleman, P. Chandra, and T. C. Lubensky, *Phys. Rev. X* **12**, 011043 (2022).
- [35] H. Li and T. Li, *Phys. Rev. B* **106**, 035112 (2022).
- [36] A.-M. Nedić, V. L. Quito, Y. Sizyuk, and P. P. Orth, *Phys. Rev. B* **107**, 184401 (2023).
- [37] J. Strockoz, D. S. Antonenko, D. LaBelle, and J. W. Venderbos, [arXiv:2211.11739](https://arxiv.org/abs/2211.11739).
- [38] J. F. Dodaro, S. A. Kivelson, Y. Schattner, X. Q. Sun, and C. Wang, *Phys. Rev. B* **98**, 075154 (2018).

- [39] J. W. F. Venderbos and R. M. Fernandes, *Phys. Rev. B* **98**, 245103 (2018).
- [40] V. Kozii, H. Isobe, J. W. F. Venderbos, and L. Fu, *Phys. Rev. B* **99**, 144507 (2019).
- [41] Y. Xu, X.-C. Wu, C.-M. Jian, and C. Xu, *Phys. Rev. B* **101**, 205426 (2020).
- [42] R. M. Fernandes and J. W. F. Venderbos, *Sci. Adv.* **6**, eaba8834 (2020).
- [43] J. Kang and O. Vafek, *Phys. Rev. B* **102**, 035161 (2020).
- [44] F. Xie, A. Cowsik, Z.-D. Song, B. Lian, B. A. Bernevig, and N. Regnault, *Phys. Rev. B* **103**, 205416 (2021).
- [45] D. V. Chichinadze, L. Classen, and A. V. Chubukov, *Phys. Rev. B* **101**, 224513 (2020).
- [46] A. O. Sboychakov, A. V. Rozhkov, A. L. Rakhmanov, and F. Nori, *Phys. Rev. B* **102**, 155142 (2020).
- [47] Y. Wang, J. Kang, and R. M. Fernandes, *Phys. Rev. B* **103**, 024506 (2021).
- [48] S. Onari and H. Kontani, *Phys. Rev. Lett.* **128**, 066401 (2022).
- [49] E. Brillaux, D. Carpentier, A. A. Fedorenko, and L. Savary, *Phys. Rev. Res.* **4**, 033168 (2022).
- [50] M. Motty and E.-A. Kim, *Nat. Commun.* **13**, 7098 (2022).
- [51] F. Grandi, A. Consiglio, M. A. Sentef, R. Thomale, and D. M. Kennes, *Phys. Rev. B* **107**, 155131 (2023).
- [52] M. Hecker and J. Schmalian, *npj Quantum Mater.* **3**, 26 (2018).
- [53] R. M. Fernandes, P. P. Orth, and J. Schmalian, *Annu. Rev. Condens. Matter Phys.* **10**, 133 (2019).
- [54] P. T. How and S.-K. Yip, *Phys. Rev. B* **100**, 134508 (2019).
- [55] A. Y. Kuntsevich, M. A. Bryzgalov, R. S. Akzyanov, V. P. Martovitskii, A. L. Rakhmanov, and Y. G. Selivanov, *Phys. Rev. B* **100**, 224509 (2019).
- [56] I. Kostylev, S. Yonezawa, Z. Wang, Y. Ando, and Y. Maeno, *Nat. Commun.* **11**, 4152 (2020).
- [57] K. Kimura, M. Sgrist, and N. Kawakami, *Phys. Rev. B* **105**, 035130 (2022).
- [58] M. Hecker and R. M. Fernandes, *Phys. Rev. B* **105**, 174504 (2022).
- [59] J. P. Straley and M. E. Fisher, *J. Phys. A: Math. Gen.* **6**, 1310 (1973).
- [60] D. Blankschtein and A. Aharony, *J. Phys. C: Solid State Phys.* **13**, 4635 (1980).
- [61] F. Y. Wu, *Rev. Mod. Phys.* **54**, 235 (1982).
- [62] H. v. Löhneysen, A. Rosch, M. Vojta, and P. Wölfle, *Rev. Mod. Phys.* **79**, 1015 (2007).
- [63] V. Oganesyan, S. A. Kivelson, and E. Fradkin, *Phys. Rev. B* **64**, 195109 (2001).
- [64] W. Metzner, D. Rohe, and S. Andergassen, *Phys. Rev. Lett.* **91**, 066402 (2003).
- [65] M. Garst and A. V. Chubukov, *Phys. Rev. B* **81**, 235105 (2010).
- [66] M. A. Metlitski and S. Sachdev, *Phys. Rev. B* **82**, 075127 (2010).
- [67] Y. Schattner, S. Lederer, S. A. Kivelson, and E. Berg, *Phys. Rev. X* **6**, 031028 (2016).
- [68] S. Lederer, Y. Schattner, E. Berg, and S. A. Kivelson, *Proc. Natl. Acad. Sci. USA* **114**, 4905 (2017).
- [69] A. Klein and A. Chubukov, *Phys. Rev. B* **98**, 220501(R) (2018).
- [70] E. C. Stoner and E. Wohlfarth, *Philos. Trans. R. Soc. London Ser., A* **240**, 599 (1948).
- [71] D. Belitz, T. R. Kirkpatrick, and J. Rollbühler, *Phys. Rev. Lett.* **94**, 247205 (2005).
- [72] M. Brando, D. Belitz, F. M. Grosche, and T. R. Kirkpatrick, *Rev. Mod. Phys.* **88**, 025006 (2016).
- [73] D. Belitz, T. R. Kirkpatrick, and T. Vojta, *Phys. Rev. Lett.* **82**, 4707 (1999).
- [74] A. V. Chubukov, C. Pépin, and J. Rech, *Phys. Rev. Lett.* **92**, 147003 (2004).
- [75] D. L. Maslov and A. V. Chubukov, *Phys. Rev. B* **79**, 075112 (2009).
- [76] H. Terletska, J. Vučićević, D. Tanasković, and V. Dobrosavljević, *Phys. Rev. Lett.* **107**, 026401 (2011).
- [77] T. Furukawa, K. Miyagawa, H. Taniguchi, R. Kato, and K. Kanoda, *Nat. Phys.* **11**, 221 (2015).
- [78] Z. Wang, D. Gautreau, T. Birol, and R. M. Fernandes, *Phys. Rev. B* **105**, 144404 (2022).
- [79] J. A. Hertz, *Phys. Rev. B* **14**, 1165 (1976).
- [80] A. J. Millis, A. J. Schofield, G. G. Lonzarich, and S. A. Grigera, *Phys. Rev. Lett.* **88**, 217204 (2002).
- [81] R. Samajdar, M. S. Scheurer, S. Turkel, C. Rubio-Verdú, A. N. Pasupathy, J. W. Venderbos, and R. M. Fernandes, *2D Mater.* **8**, 034005 (2021).
- [82] D. E. Parker, T. Soejima, J. Hauschild, M. P. Zaletel, and N. Bultinck, *Phys. Rev. Lett.* **127**, 027601 (2021).
- [83] A. V. Maharaj, E. W. Rosenberg, A. T. Hristov, E. Berg, R. M. Fernandes, I. R. Fisher, and S. A. Kivelson, *Proc. Natl. Acad. Sci. USA* **114**, 13430 (2017).
- [84] M. A. Metlitski, D. F. Mross, S. Sachdev, and T. Senthil, *Phys. Rev. B* **91**, 115111 (2015).
- [85] A. Klein, S. Lederer, D. Chowdhury, E. Berg, and A. Chubukov, *Phys. Rev. B* **97**, 155115 (2018).
- [86] S.-S. Lee, *Annu. Rev. Condens. Matter Phys.* **9**, 227 (2018).
- [87] O. Vafek, *arXiv:2209.08208*.
- [88] Z. Zheng, Q. Ma, Z. Bi, S. de La Barrera, M.-H. Liu, N. Mao, Y. Zhang, N. Kiper, K. Watanabe, T. Taniguchi *et al.*, *Nature (London)* **588**, 71 (2020).
- [89] D. Blankschtein, Y. Shapir, and A. Aharony, *Phys. Rev. B* **29**, 1263 (1984).
- [90] R. M. Fernandes and L. Fu, *Phys. Rev. Lett.* **127**, 047001 (2021).